Multiscale modelling of soft lattice metamaterials: micromechanical nonlinear buckling analysis, experimental verification, and macroscale constitutive behaviour

M. Jamshidian, N. Boddeti, D. W. Rosen, O. Weeger

Accepted manuscript published in

International Journal of Mechanical Sciences

105956 (2020)

DOI 10.1016/j.ijmecsci.2020.105956

Multiscale modelling of soft lattice metamaterials: micromechanical nonlinear buckling analysis, experimental verification, and macroscale constitutive behaviour

M. Jamshidian[1]*, N. Boddeti[1,2], D. W. Rosen[1,3], O. Weeger[1,4]

[1] Singapore University of Technology and Design, Digital Manufacturing and Design Centre, 8 Somapah Road, Singapore 487372, Singapore

[2] Washington State University, School of Mechanical and Materials Engineering, PO BOX 642920, Pullman, WA 99164-2920, United States

[3] Georgia Institute of Technology, George W. Woodruff School of Mechanical Engineering, 801 Ferst Drive, Atlanta, GA 30332-0405, United States

[4] Technical University of Darmstadt, Cyber-Physical Simulation Group, Dolivostraße 15, 64293 Darmstadt, Germany

*corresponding author: mostafa_jamshidian@sutd.edu.sg

Abstract

Soft lattice structures and beam-metamaterials made of hyperelastic, rubbery materials undergo large elastic deformations and exhibit structural instabilities in the form of micro-buckling of struts under both compression and tension. In this work, the large-deformation nonlinear elastic behaviour of beam-lattice metamaterials is investigated by micromechanical nonlinear buckling analysis. The micromechanical 3D beam finite element model uses a primary linear buckling analysis to incorporate the effect of geometric imperfections into a subsequent nonlinear post-buckling analysis. The micromechanical computational model is validated against tensile and compressive experiments on a 3D-printed sample lattice structure manufactured via multi-material jetting. For the development and calibration of macroscale continuum constitutive models for nonlinear elastic deformation of soft lattice structures at finite strains, virtual characterization tests are conducted to quantify the effective nonlinear response of representative unit cells under periodic boundary conditions. These standard tests, commonly used for hyperelastic material characterization, include uniaxial, biaxial, planar and volumetric tension and compression, as well as simple shear. It is observed that besides the well-known stretch- and bending-dominated behaviour of cellular structures, some lattice types are dominated by buckling and post-buckling response. For multiscale simulation based on nonlinear homogenization, the uniaxial standard test results are used to derive parametric hyperelastic constitutive relations for the effective constitutive behaviour of representative unit cells in terms of lattice aspect ratio. Finally, a comparative study for compressive deformation of a sample sandwich lattice structure simulated by both full-scale beam and continuum finite element models shows the feasibility and computational efficiency of the effective continuum model.

Keywords: Lattice structures, Multiscale modelling, Micromechanics, Nonlinear buckling analysis, Hyperelastic constitutive model

1. Introduction

Additive and other advanced manufacturing methods now enable the fabrication of metamaterials with cellular microstructures, which can not only realize high stiffness-to-density ratios, but also tailored spatially-varying stiffness, anisotropy, density, or functional behaviour as well as multi-physical characteristics [1, 2]. In engineering applications of lattice structures, i.e. cellular materials with truss- or beam-like microstructure, the focus has so far been largely on lightweight load-carrying parts in applications like aerospace industry and medical implants. Such lattice structures can be precisely fabricated through metal 3D printing processes like selective laser melting (SLM) and electron beam melting (EBM) [3], or polymer 3D printing via stereolithography (SLA) and selective laser sintering (SLS). The mechanical performance of these *stiff* lattice structures is characterized by small deformation, linear elastic and plastic behaviour, as well as fracture and failure. Most of the modelling and simulation studies as well as commercial computer-aided design (CAD) tools focus on these stiff lattice structures [4, 5, 6, 7, 8, 9, 10].

Recently there has been increasing interest in the fabrication and application of *soft* lattices and metamaterials which can achieve large elastic deformations [11, 12], exploit mechanical instabilities and buckling [13, 14], recoverably absorb energy and mitigate vibrations [15], exhibit auxetic behaviour [16, 17, 18], have thermally tuneable and self-healing properties [19], or shape-memory and shape-morphing abilities [20, 21]. Mechanical modelling of such soft lattice structures involves large deformations and finite strains and in particular recoverable elastic buckling of some struts followed by their post-buckling and bending behaviour [22]. While buckling and instabilities generally lead to failure of stiff lattices due to the resulting high strains and stresses, soft lattices can exploit buckling-dominated behaviour since moderately large elastic strains can be accommodated by hyperelastic materials.

In general, for multiscale modelling approaches of periodic cellular materials, the effective behaviour of a microstructure is homogenized based on a representative volume element (RVE) or a periodically repeated unit cell (RUC) [23, 24, 25]. For open-cell beam-lattice structures, their effective properties such as linear elastic moduli, scale with the microstructure aspect ratio defined as the ratio of strut diameter to the unit cell length. Depending on the microarchitecture and loading scenario, stretching- and bending-dominated behaviours have been frequently characterized in previous studies [23, 24, 26, 27]. Furthermore, previous research has shown that the modelling of perfect as-designed lattices often over-estimates the mechanical response of physical manufactured structures [28, 22]. The difference is attributed to the geometric imperfections that facilitate buckling and failure. The investigation of buckling behaviour usually involves the analysis of buckling loads and post-buckling behaviour [29]. Buckling loads and patterns have already been studied for various 2D beam-lattices and metamaterials [30, 31]. Furthermore, buckling and post-buckling response of beam-lattices under compressive loading conditions have been investigated [32, 33, 34]. To exploit the buckling phenomena, optimized periodic imperfections were applied on strut diameter of Kagome lattices [35].

In the present study, we are interested in multiscale analysis of the large-deformation elastic response of soft beam-lattice structures that involves pre- and post-buckling behaviour. For this purpose, a nonlinear buckling analysis is performed in which the linear buckling modes are applied on the lattices as geometric imperfections [29]. The mechanical response of soft lattices is modelled by nonlinear shear-deformable 3D beam finite elements which are commonly used for slender structures with moderate aspect ratios. Since rubbery materials with elastic behaviour at finite

deformations are considered, plasticity effects are not included in the microscale analysis of beam models. The effective large deformation response of various lattice types is obtained by applying this approach to the corresponding unit cells under different loading conditions in accordance with standard hyperelastic material characterization tests including uniaxial, biaxial, planar, and volumetric tension and compression, as well as simple shear. As will be shown later, this effective behaviour in the finite strain regime can be dominated by the effects of buckling and postbuckling, and hence yield vastly different responses in tensile and compressive loading scenarios.

Since invoking micromechanical nonlinear buckling analyses within a concurrent multiscale simulation, e.g. as part of a FE^2 scheme, is computationally expensive, most multiscale simulations are sequential and based on the formulation of closed-form effective constitutive models which are however challenging for nonlinear problems [36]. So far, nonlinear constitutive models and similar theories have been developed only for simple 2D lattice metamaterials [37, 38, 39, 40]. As a step towards nonlinear homogenization, we explore the application of hyperfoam constitutive model which is principally developed for large deformation of rubbery foams [41, 42, 43]. Furthermore, to enable multiscale design of lattice structures with graded properties via topology optimization, which has been realized so far only for linear 2D and 3D lattice structures [44, 45], we parameterize the hyperfoam constitutive model in terms of the lattice aspect ratio as a design variable.

The structure of the present manuscript and the developed multiscale computational framework are visualized in the graphical abstract and briefly outlined as follows. In Section 2, the computational model for the nonlinear buckling analysis of soft lattice structures is introduced and experimentally validated. In Section 3, the implementation of the homogenization method for lattice unit cells is presented and the micromechanical analysis is performed to extract the effective behaviour of various unit cell types. In Section 4, the extracted data is used to formulate a parameterized macroscale hyperfoam constitutive model that reproduces the nonlinear elastic response of soft lattices under uniaxial loading. To demonstrate the applicability and computational efficiency of the macroscale hyperfoam model, full-scale beam and multiscale continuum finite element simulations are compared for compression of a sample sandwich lattice structure in Section 5. Finally, the findings are summarized, and a conclusion is provided in Section 6.

2. Computational model and experimental validation

For the computational modelling of large deformations of soft lattices, a nonlinear buckling analysis is employed, as implemented in the Abaqus finite element package. The employed computational approach for soft lattice modelling is summarized in Fig. 1. First, the perfect lattice structure is modelled using nonlinear 3D beam elements. Then, under prescribed boundary conditions and loads, a linear buckling analysis is preformed to obtain the buckling modes and the corresponding buckling loads. The buckling mode shapes are then incorporated into the model as initial geometric imperfections. These so-called *imperfection mode shapes* are multiplied by a so-called *imperfection factor* to perturb the perfect structure. Particularly, the linear combination of the imperfection mode shapes with the imperfection factor as the coefficients allows the modelling of deviations from the designed geometry involved in the printing process. The structural deformation of the imperfect lattice under the prescribed boundary conditions is then simulated to obtain the nonlinear post-buckling load-deformation response of the structure. The total number of imperfection mode shapes $N_\circ$ is determined by a post-buckling convergence analysis. The imperfection factor $\lambda_\circ$ represents the average of all geometric imperfections and can be related to the manufacturing process precision.

The imperfection factor is calibrated to the experimental structural load-displacement response of the lattice structure.

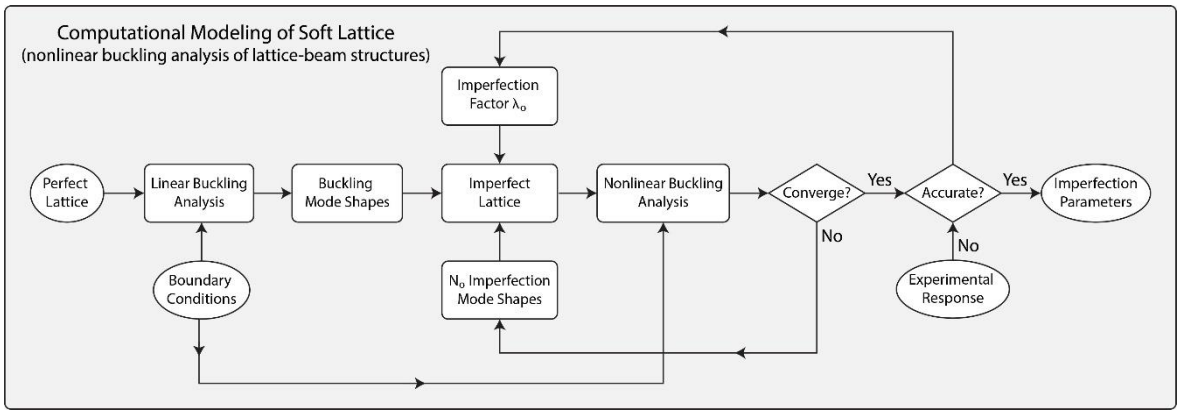

Fig. 1. Computational approach for modelling large deformation behaviour of soft lattices based on 3D beam modelling and nonlinear buckling analysis

2.1. Modelling of a sample lattice structure

To further elaborate on the proposed computational approach and the parameters involved, detailed modelling of a sample lattice structure is presented in this section. In order to estimate the imperfection factor λ_o and to verify the validity of the proposed computational framework for the modelling of the large deformation response of lattice structures, simulation and experimental results are compared for the sample lattice structure as shown in Fig. 2.

A structure composed of $2 \times 2 \times 2$ body-centred cubic (BCC) unit cells of size $15 \times 15 \times 15\ mm^3$ with a strut radius of $0.75\ mm$, i.e. an aspect ratio of 0.1, is created as shown in wireframe representation in Fig. 2a. The lattice is 3D printed with Tango+ material on a Stratasys J750 PolyJet printer which is a voxel-based multimaterial jetting machine with a voxel resolution of 42×84×27 µm. The material properties of Tango+ were characterized by uniaxial tensile testing of 3D printed dog bone samples according to ASTM D412 standard. The Tango+ material is well described by a linear elastic material model with Young's modulus of $E = 0.53\ MPa$ and Possion's ratio of $\nu = 0.49$. For compression and tensile experiments of the 3D printed lattice structure, two top and bottom clamps are printed with the much stiffer VeroMagenta material ($E > 1\ GPa$) together with the lattice as shown in Fig. 2b. The final printed sample used in mechanical testing is shown in Fig. 2c.

The wireframe model of the lattice in Fig. 2 is imported into Abaqus and meshed with quadratic, 3-node nonlinear 3D Timoshenko beam elements; termed B32 in Abaqus. Each node in these elements has six degree of freedoms (DOFs) including three displacement DOFs and three rotation DOFs. An isotropic linear elastic material model with Young's modulus of $E = 0.53\ MPa$ and Possion's ratio of $\nu = 0.49$ is used to define beam sections with circular profiles. The Tango+ material density is $\rho = 1120\ kg/m^3$. A global element size of 1 mm has shown to satisfy mesh convergence analysis in all simulations reported in this study. Fig. 2d shows the computational model of the perfect lattice structure considering joint stiffening by the approach introduced in [22]. This approach increases the radii of the beam elements adjacent to nodes to consider the additional stiffness of the bulky and thus more rigid joints caused by overlapping and smoothing effects of the node geometries.

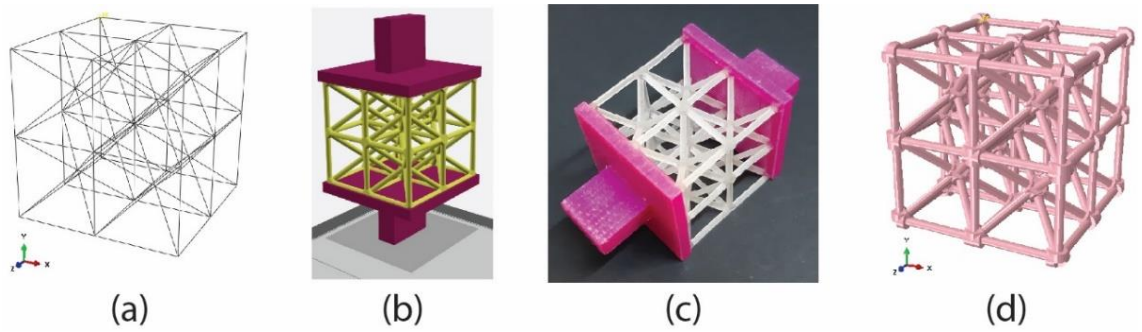

Fig. 2. A sample soft lattice structure used for the validation of the computational model and the estimation of the imperfection factor: (a) Wireframe model of a $2 \times 2 \times 2$ BCC lattice structure. (b) 3D print model with assigned materials; Tango+ (yellow) for lattice and VeroMagenta (magenta) for top and bottom clamps. (c) 3D printed sample used in experiments. (d) Computational model of lattice meshed with beam elements and assigned beam section profiles considering joint stiffening.

For simulating the uniaxial tension or compression of the lattice between the rigid top and bottom plates, all DOFs for all nodes on the top surface are constrained to a top reference node. Similarly, all DOFs of all nodes on the bottom surface are constrained to a bottom reference node. These constraints ensure that the actual effect of the rigid plates is incorporated in the simulations. The bottom reference node is fully clamped by constraining all its DOFs. All DOFs of the top reference node except its vertical displacement DOF are constrained. The free vertical displacement DOF is used to apply uniaxial tensile/compressive deformation.

2.2. Linear buckling analysis

In order to perform a linear buckling analysis, a compressive load of $1\ N$ is applied to the vertical free DOF of the top reference node. The buckling loads for the first 100 buckling mode shapes under uniaxial compression are then computed as plotted in Fig. 3a. For illustration purposes, the buckling mode shapes 1, 9, 17 and 75 are also displayed in Fig. 3b. For buckling mode shapes with positive buckling load, e.g., mode shapes 1, 9 and 17, buckling of vertical struts under compressive vertical loading is obvious. However, for buckling mode shape 75 with a negative buckling load, lateral buckling of the horizontal struts normal to the loading direction happens in tensile vertical loading.

For linear buckling analysis under compressive loading, positive buckling load mode shapes are used as imperfections for the nonlinear buckling analysis in compressive deformation. Similarly, the mode shapes with negative buckling load are incorporated as imperfections in nonlinear buckling analysis of tensile deformation. For a linear buckling analysis under compressive loading, the number of imperfection mode shapes $N_\circ$ denotes either the first $N_\circ$ positive buckling load mode shapes in compressive deformation or the first $N_\circ$ negative buckling load mode shapes in tensile deformation in the subsequent nonlinear buckling analysis.

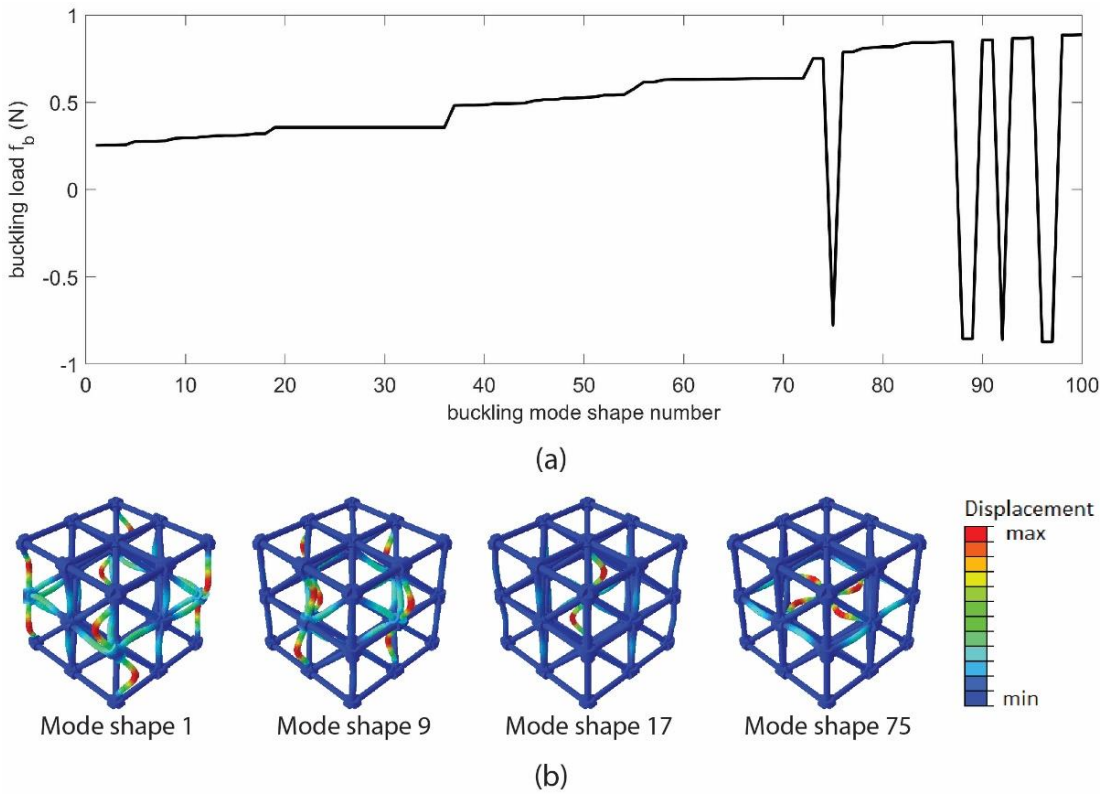

Fig. 3. Linear buckling analysis for the sample BCC lattice structure from Fig. 2: (a) Buckling loads for the first 100 buckling mode shapes under uniaxial compression loading. (b) Buckling mode shapes 1, 9, 17, 75 are displayed as examples. Mode 75 is the first negative load (tensile) buckling mode shape.

2.3. Nonlinear buckling analysis: Compressive loading

Following the extraction of buckling mode shapes under compressive loading, the imperfection mode shapes are used to construct the imperfect lattice structure shown in Fig. 4. Then, the post-buckling nonlinear response of the imperfect lattice under uniaxial compression is obtained by incrementally applying a compressive displacement boundary condition of $6\ mm$ on the free DOF of the top reference node. The total deformation is applied over a time step of $1\ s$ with linear variation of displacement boundary conditions over time. The simulation begins by an Abaqus/Standard Static analysis including geometric nonlinearity with automatic incrementation size. At some point when the lattice deformation is very large, the static simulation may not converge and will terminate even with very small increment sizes. In this case, an Abaqus/Standard Dynamic analysis is used after the static analysis to automatically continue the simulation. The dynamic analysis uses an automatic incrementation size and begins with an initial increment size of $10^{-5}\ s$ to ensure a very smooth transition from static to dynamic analysis. Though with lower computational efficiency, the dynamic analysis allows the completion of the whole step time to the end. The very negligible kinetic energy in comparison with the internal energy in the dynamic analysis ensures a quasit static simulation of the lattice deformation using a dynamic analysis.

The total number of imperfection mode shapes $N_\circ$ is to be determined by a convergence analysis. At a fixed value of the imperfection factor $\lambda_\circ$, the convergence analysis involves the extraction of structural load-displacement responses for increasing values of $N_\circ$. The minimum value of $N_\circ$ for

which the nonlinear load-displacement response converges, is considered as the necessary value for $N_\circ$.

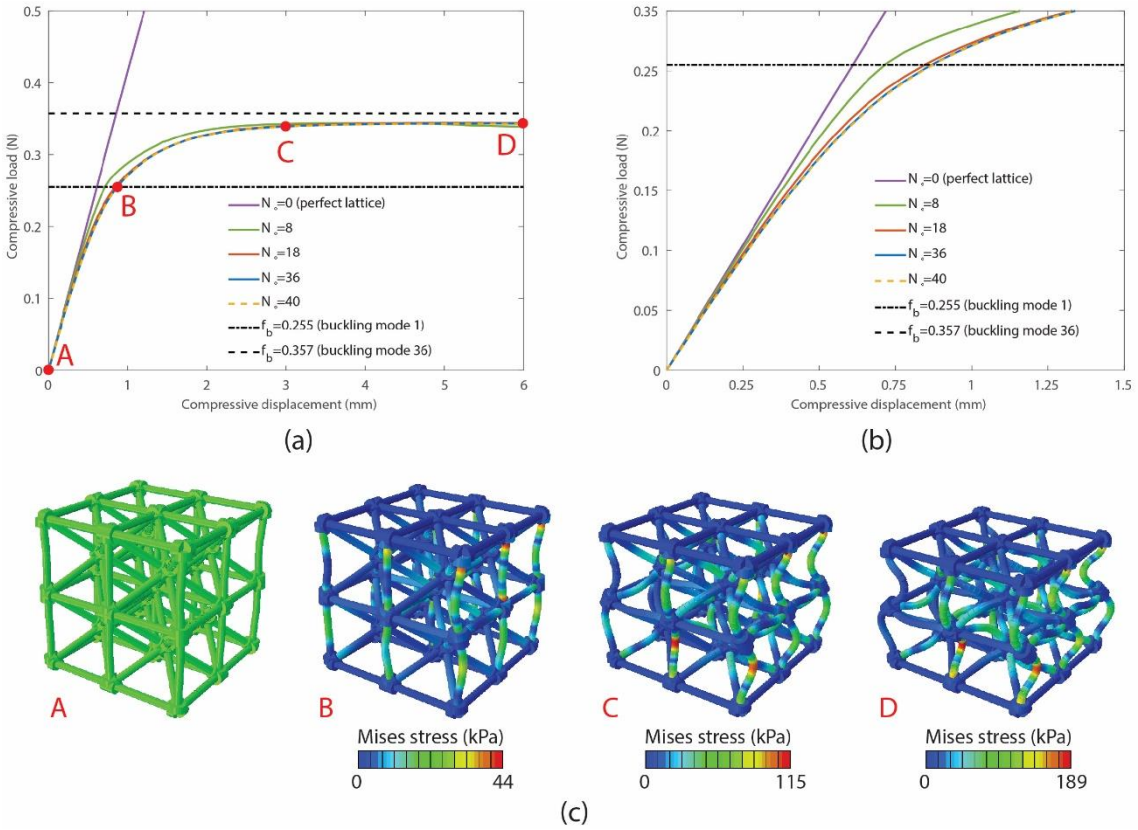

Fig. 4. Nonlinear buckling analysis for compression of the sample BCC lattice structure from Fig. 2. (a) The convergence analysis is performed for an imperfect lattice structure with a typical imperfection factor $\lambda_\circ = 0.075\ mm$. (b) Convergence is reached for an imperfect lattice structure with total number of imperfection mode shapes $N_\circ = 36$. (c) The deformed shape of the imperfect lattice at different points B, C, D corresponding to the compressive displacements $0.84\ mm$, $3\ mm$ and $6\ mm$ show the buckling of vertical struts.

The convergence analysis for the typical imperfection factor $\lambda_\circ = 0.075$ is shown in Fig. 4a. At a first glance, the dramatic difference between the responses of the perfect lattice and imperfect lattices is obvious. For the perfect lattice, the load increases linearly with displacement much higher above the first buckling load. At some point not shown in Fig. 4a, the Newton-Raphson iterations cannot converge, probably due to a sudden very large buckling response, and hence simulation is terminated. Without any comparison with experiments, the perfect lattice response is clearly shown to be an overestimation of the actual lattice response as the load goes much beyond the buckling load of the initial buckling mode shapes.

As shown in Fig. 4a, the imperfect lattice with various values of $N_\circ$ demonstrates an initial stiffness almost identical to the perfect lattice stiffness. By increasing the compressive displacement, the load-displacement response of the imperfect lattice deviates from and falls below the initially linear response. Such a deviation from linearity becomes obvious around the lowest buckling load of $f_b = 0.255\ N$ corresponding to buckling mode 1. At this load level, identified by point B in Fig. 4a, the buckling of vertical struts becomes visible. The rate of load drop increases by further increase of the compressive displacement and the load asymptotically approaches a plateau at point C in Fig. 4a.

The load remains constant with further increase of the compressive displacement from points C to D in Fig. 4a. Overall, the simulated load-displacement response of the imperfect lattice resembles the typical experimental nonlinear buckling curves of soft lattices in [22].

In order to clearly observe the convergence of the nonlinear buckling response, it is magnified around the buckling region as shown in Fig. 4b. While increasing $N_\circ$ from 8 to 40, the structural response converges, as the difference between the successive curves becomes negligible. Particularly, there is almost no difference between the curves for $N_\circ$ values of 36 and 40. Hence, we set the number of imperfection mode shapes to $N_\circ = 36$ for compressive loading test.

In order to investigate the effect of the imperfection factor on the nonlinear buckling response of the lattice structure, load-displacement curves are plotted in Fig. 5 for three imperfection factors $\lambda_\circ = 0.025$, $\lambda_\circ = 0.075$, and $\lambda_\circ = 0.150$ with a fixed value of the number of imperfection mode shapes $N_\circ = 36$. As illustrated by Fig. 5, a higher imperfection factor decreases the structure's initial stiffness and smoothens the transition from linear deformation to nonlinear buckling response. However, it has a mild effect on decreasing the level of the post-buckling load plateau. Overall, Fig. 5 implies that the nonlinear buckling response of the lattice is not very sensitive to the imperfection factor. In other words, increasing the imperfection factor by 6 times from $\lambda_\circ = 0.025$ to $\lambda_\circ = 0.150$, the structural response variation remains less than 20%. While the imperfection factor can be well approximated by the 3D printing precision, its precise value is to be determined by calibrating the simulation results to the experimental structural response.

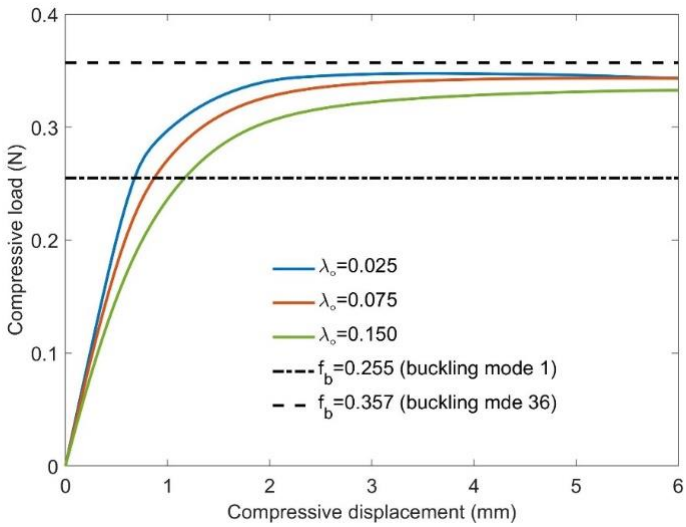

Fig. 5. Effect of imperfection factor on the nonlinear buckling behaviour of the sample BCC lattice structure from Fig. 2 under uniaxial compression. The load-displacement curves are plotted for three imperfection factors $\lambda_\circ = 0.025$, $\lambda_\circ = 0.075$, and $\lambda_\circ = 0.150$ with a fixed value of the number of imperfection mode shapes $N_\circ = 36$.

2.4. Nonlinear buckling analysis: Tensile loading

To simulate the tensile response of the lattice structure, the buckling mode shapes with negative buckling loads are used as imperfection mode shapes. The convergence analysis of the tensile loading test is shown in Fig. 6 for the typical imperfection factor $\lambda_\circ = 0.075$. The tensile load-

displacement response in Fig. 6a illustrates a linear behaviour. Such a linear curve with no sign of buckling arises from the fact that the tensile deformation of lattice is dominated by stretching of vertical struts along the loading direction. The lateral buckling of struts due to the lateral contraction of the lattice structure, which can be observed in Figs. 6b and 6c, has no manifestation on the structural load-displacement response.

As shown in Fig. 6a, while the perfect lattice is slightly stiffer than the imperfect lattices in tension, the convergence analysis for the tensile load response is insensitive to the number of imperfection mode shapes when increasing $N_\circ$ from 3 to 12. However, our simulations show that the inclusion of imperfection mode shapes is required to get proper lateral contraction, as can be seen in Fig. 6b. The lateral contraction of the lattice structure is calculated as the total thinning on its symmetry plane normal to the tensile loading direction. As shown in Fig. 6b, the nonlinear lateral contraction of the imperfect lattices is considerably higher than the lateral contraction of the perfect lattice. The convergence analysis in Fig. 6b is performed by increasing $N_\circ$ from 3 to 12 and shows that the lateral contraction response converges for $N_\circ = 9$. Hence, the number of imperfection mode shapes is set to $N_\circ = 9$ for tensile loading tests. The deformed shapes of the imperfect lattice during tensile loading shown in Fig. 6c illustrate that the lateral contraction is dominated by the buckling of the horizontal struts normal to the tensile loading direction.

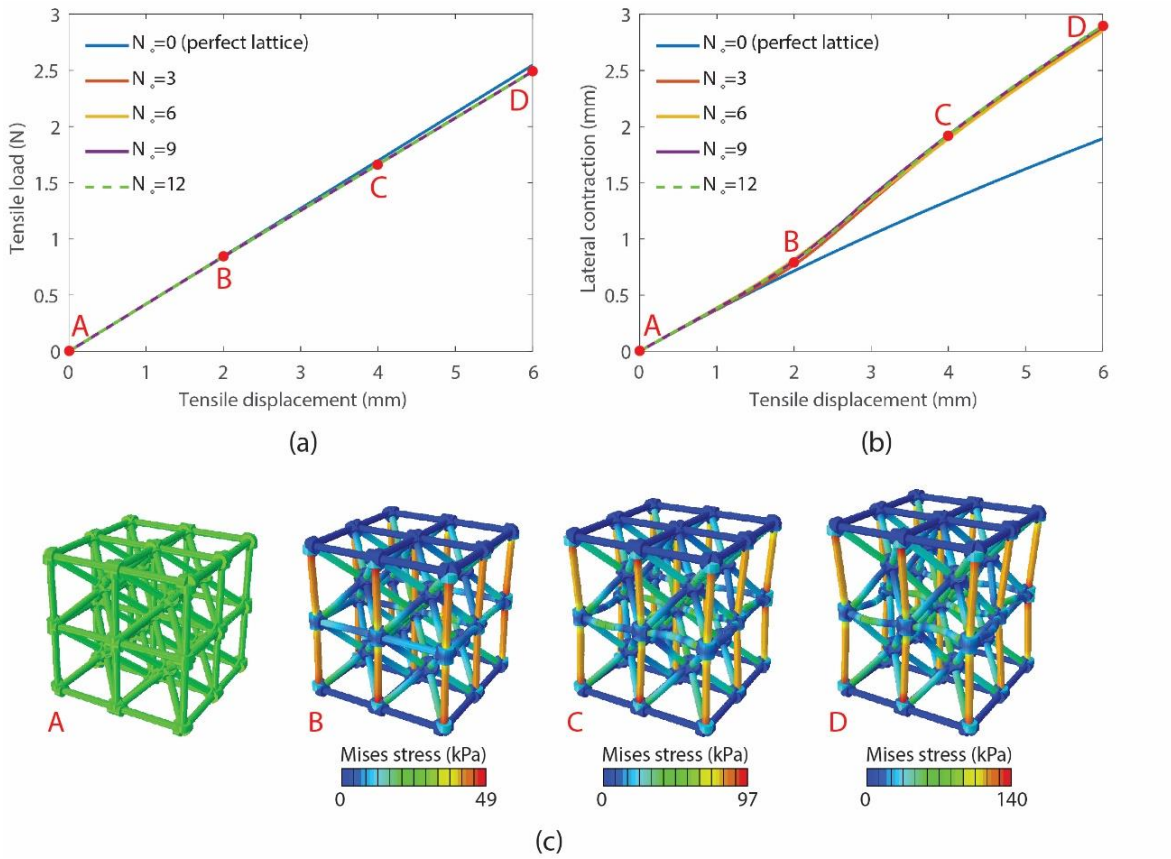

Fig. 6. Nonlinear buckling analysis for tension of the sample BCC lattice structure from Fig. 2. The convergence analysis is performed based on both (a) the tensile load response and (b) the lateral contraction response of the imperfect lattice with the imperfection factor $\lambda_\circ = 0.075\ mm$. Convergence is reached for an imperfect lattice structure with total number of imperfection mode shapes $N_\circ = 9$. (c) The deformed shape of the imperfect lattice at different points B, C, D

corresponding to the tensile displacements $2\,mm$, $4\,mm$ and $6\,mm$ shows lateral buckling of horizontal struts.

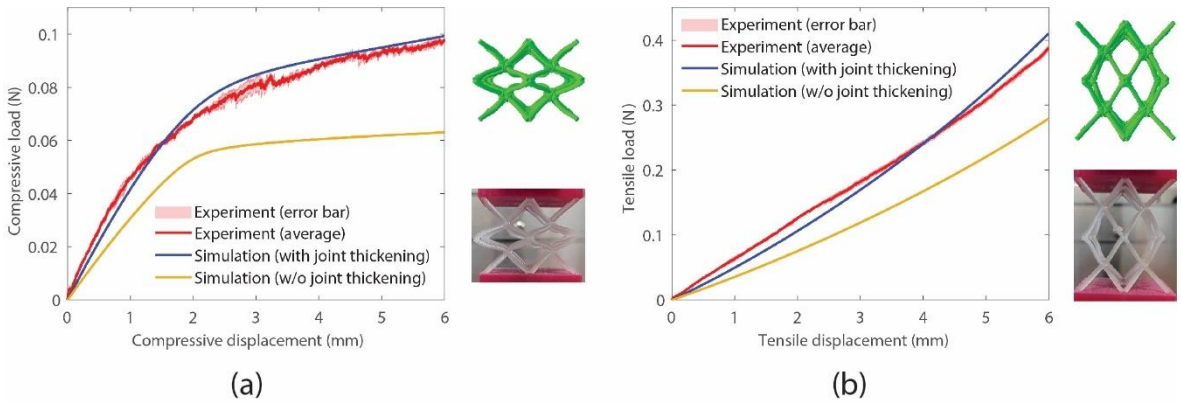

Fig. 7. Comparison between experimental and simulation results for the nonlinear buckling load-displacement response of a bending-dominated lattice structure composed of $2 \times 2 \times 2$ BC unit cells of cell size $15 \times 15 \times 15\,mm^3$ and strut radius $0.75\,mm$, 3D printed with Tango+ material. (a) Uniaxial compressive response and lattice morphology under the compressive displacement $3\,mm$. (b) Uniaxial tensile response and lattice morphology under the tensile displacement $3\,mm$.

2.5. Experimental validation

For the validation of the proposed computational framework and for the precise determination of the imperfection factor, 3D printed samples were experimentally tested in uniaxial deformation. A two-step validation procedure using two different lattice structures is used as follows. In the first validation step, a bending-dominated lattice structure with no strut buckling in either tension or compression is used. The purpose is to exclude the effect of nonlinear buckling related parameters and set the primary computational parameters such as element type, mesh size, time increment, etc. Being confident with all the primary computational parameters, in the second validation step a buckling-dominated lattice structure with strut buckling in both tension and compression is used to calibrate the imperfection factor.

Fig. 7 shows the experimental and simulation results for the load-displacement response of a bending-dominated lattice structure composed of $2 \times 2 \times 2$ body-centred, BC unit cells of cell size $15 \times 15 \times 15\,mm^3$ and strut radius $0.75\,mm$, 3D printed with Tango+ material. As shown in Fig. 7, the simulated response of the BC lattice structure agrees well with the corresponding experimental curve in both tension and compression. Also, the qualitative comparison of the deformation between the simulation and experiments reveals a close match.

Fig. 8 illustrates the experimental and simulation results for the nonlinear buckling load-displacement response of a buckling-dominated lattice structure composed of $2 \times 2 \times 2$ BCC unit cells of cell size $15 \times 15 \times 15\,mm^3$ and strut radius $0.75\,mm$, 3D printed with Tango+ material. For the uniaxial compressive response, a good correspondence between the simulation and experimental response is achieved with an imperfection factor $\lambda_\circ = 0.075\,mm$ as shown in Fig. 8a. It is noteworthy that the simulated response is the converged curve with $N_\circ = 36$. The calibrated value for imperfection factor is well within the range of the accuracy of the 3D printing machine,

since the Stratasys PolyJet printer has a voxel size of $0.042 \times 0.084 \times 0.027\ mm^3$. Hence, the imperfection factor $\lambda_\circ = 0.075\ mm$ has been used in all the simulations presented in this paper. The tensile response in Fig. 8b also shows a good correspondence between simulations and experiments.

To ensure experimental repeatability, two samples where printed for each of the BC and BCC lattice structures and each uniaxial deformation test was performed three times on each sample. The shaded error bar area of the experimental responses in Figs. 7 and 8 demonstrates the experimental repeatability.

In order to highlight the effect and show the necessity of joint thickening in soft lattices modelling, the simulated load-displacement responses of lattices without joint thickening are also plotted in Figs. 7 and 8. The comparison between the simulated responses with and without joint thickening clearly shows that the response of the lattice structures is underestimated without joint stiffening.

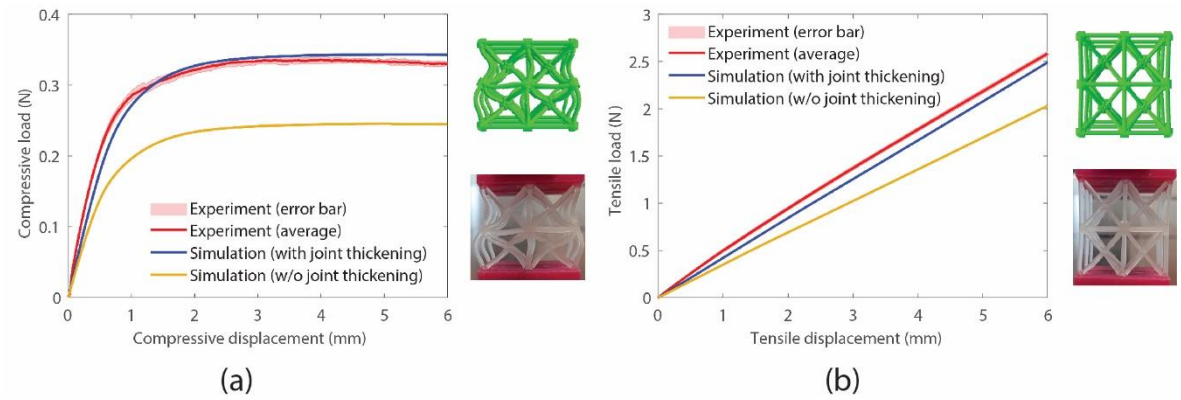

Fig. 8. Comparison between experimental and simulation results for the nonlinear buckling load-displacement response of a buckling-dominated lattice structure composed of $2 \times 2 \times 2$ BCC unit cells of cell size $15 \times 15 \times 15\ mm^3$ and strut radius $0.75\ mm$ 3D printed with Tango+ material. (a) uniaxial compressive response and lattice morphology under the compressive displacement $3\ mm$. (b) uniaxial tensile response and lattice morphology under the tensile displacement $3\ mm$.

3. Micromechanical analysis of the effective behaviour of soft lattices

Having introduced and validated the computational method for the analysis of the nonlinear buckling response of lattice structures and its essential parameters, the number of imperfection modes and the imperfection factor, now the effective behaviour of different types of lattice structures shall be investigated by micromechanical analysis of the lattice unit cells. The general idea of micromechanics and multiscale simulation is that a heterogeneous structure, here a lattice structure, can be macroscopically modelled as a continuum and that the effects of its microstructure can be considered within the macroscopic constitutive model i.e. the relationship between effective strain and effective stress [36, 46]. In such a hierarchical multiscale framework, the macroscopic deformation gradient is extended to a microscopic unit cell in terms of displacement boundary conditions on unit cell nodes. The nonlinear mechanical response of the unit cell is then computed with the proposed micromechanical computational model. The reaction forces at unit cell nodes are used to calculate the homogenized unit cell response in terms of the effective stresses. Finally, the macroscopic continuum constitutive model is calibrated using the effective stress-strain response of the unit cell.

3.1. Homogenization with periodic boundary conditions

To characterize the effective response of a unit cell under large deformations and instabilities, the deformation gradients of various standard tests are applied onto the unit cell using periodic boundary conditions and then its effective homogenized responses are extracted. The standard tests for characterizing a hyperfoam material include uniaxial tension and compression, biaxial tension and compression, planar tension and compression, volumetric compression and simple shear, which are commonly used for the (experimental or numerical) characterization of nonlinear hyperelastic materials.

The deformation gradient for uniaxial, biaxial, planar and volumetric tests is denoted by

$$\boldsymbol{F} = \begin{bmatrix} \lambda_1 & 0 & 0 \\ 0 & \lambda_2 & 0 \\ 0 & 0 & \lambda_3 \end{bmatrix},$$

where λ_1, λ_2, λ_3 are the principal stretches along the principal axes x, y, z, respectively. The principal stretches are defined as $\lambda_i = 1 + \epsilon_i$, where ϵ_i is the corresponding nominal normal strain. Denoting a prescribed stretch by $\hat{\lambda}$, the standard tests are defined as:

(i) Uniaxial test: $\lambda_1 = \hat{\lambda}$ and $\lambda_2 = \lambda_3$,
(ii) Biaxial test: $\lambda_1 = \lambda_2 = \hat{\lambda}$,
(iii) Planar test: $\lambda_1 = \hat{\lambda}$ and $\lambda_2 = 1$,
(iv) Volumetric test: $\lambda_1 = \lambda_2 = \lambda_3 = \hat{\lambda}$.

In these tests, $\hat{\lambda} > 1$ denotes tensile deformation, while $\hat{\lambda} < 1$ denotes compressive deformation. A prescribed stretch $\lambda_\circ$ is related to the corresponding nominal normal strain $\hat{\epsilon}$ by $\hat{\lambda} = 1 + \hat{\epsilon}$.

For the simple shear test, the deformation gradient is

$$\boldsymbol{F} = \begin{bmatrix} 1 & \hat{\gamma} & 0 \\ 0 & 1 & 0 \\ 0 & 0 & 1 \end{bmatrix},$$

where $\hat{\gamma}$ is the nominal shear strain in the shearing plane xy.

For simplicity, the procedure for applying periodic boundary conditions (PBC) on the X unit cell in Abaqus is explained here. This method is essentially applicable to other unit cell types with minor differences. For the sake of conciseness, such details are not presented here. We consider a generic cubic unit cell with node numbers 1 to 8 shown in Table 1. Using Timoshenko beam elements in three-dimensional space, each node has six DOFs, including three translational DOFs and three rotational DOFs. For each node, the translational DOFs U1, U2, U3 denote nodal translation along axis x, y, z, respectively, and rotational DOFs U4, U5, U6 denote nodal rotation about axis x, y, z, respectively. Hence, $U_{DOF}^{N(i)}$ represents a particular DOF of node i denoted by $N(i)$. To impose PBC on a unit cell, some reference points with the same set of DOFs as those of the nodes are created. Let $U_{DOF}^{RP(i)}$ represent a particular DOF of reference point i denoted by $RP(i)$. PBC are imposed to the unit cell by defining proper kinematic constraints among DOFs of the unit cell nodes. The constraints are imposed as defined in Table 1.

To prevent rigid body motion of the unit cell in standard tests, selected nodes are properly connected to the ground by linear springs. The definition of the ground-spring boundary conditions is given in Table 2. It is worthy of mentioning that for preventing rigid body motion, zero displacement boundary conditions are not technically applicable as the required DOFs are already inactive by implementing the constraint definitions in Table 1. Theoretically, the springs stiffness is to be infinite to apply zero displacement boundary conditions. As infinity is relative in numerical computations, the spring stiffness in set to $k_s = 10^6 N/m$ for all ground-spring connections. Such a relatively large stiffness along with relatively small spring forces f_s involved in soft lattice deformation, result in the almost zero displacements at the selected nodes.

Standard tests are run in a strain-controlled manner via displacement boundary conditions as listed in Table 3. In uniaxial, biaxial, planar and volumetric tests, the displacement boundary condition $\delta_\circ$ is applied to impose a nominal normal strain $\epsilon_\circ = \delta_\circ / l_\circ$ where $l_\circ$ is the unit cell size. In these tests, $\delta_\circ > 0$ means tensile strain and $\delta_\circ < 0$ means compressive strain. In shear test, the displacement boundary condition $\delta_\circ$ is applied to impose a nominal shear strain $\gamma_\circ = \delta_\circ / l_\circ$.

Table 1. Constraint definitons in Abaqus for standard tests under periodic boundary condition on X unit cell.

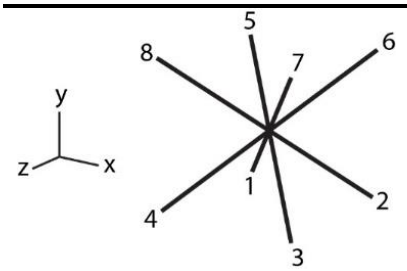

Constraint definition: $U_{DOF}^{N(i)} - U_{DOF}^{N(j)} = U_{DOF}^{RP(k)}$

i	j	k	DOF	Applicable to tests
2	1	1	1	All
3	4	1	1	All
6	5	1	1	All except shear
7	8	1	1	All except shear
5	1	2	2	All
6	2	2	2	All
7	3	2	2	All
8	4	2	2	All
4	1	3	3	All
3	2	3	3	All
7	6	3	3	All
8	5	3	3	All

Constraint definition: $U_{DOF}^{N(i)} = U_{DOF}^{RP(j)}$

i	j	DOF	Applicable to tests
5, 6, 7, 8	5	1	Only shear

Constraint definition: $U_{DOFi}^{RP(i)} = U_{DOFj}^{RP(j)}$

i	j	DOFi	DOFj	Applicable to tests

2	3	2	3	Only uniaxial

Constraint definition: $U_{DOF}^{N(i)} = U_{DOF}^{RP(k)}$			
i	k	DOF	Applicable to tests
1, …, 8	4	4	All
1, …, 8	4	5	All
1, …, 8	4	6	All

Table 2. Ground-spring boundary conditions in standard tests for preventing rigid body motion of the unit cell under PBC.

Ground-spring boundary condition definition: $k_s U_{DOF}^{N(i)} = f_s$		
i	DOF	Applicable to tests
1, 4	1	All
5, 8	1	All except shear
1, 2, 3, 4	2	All
1, 2, 5, 6	3	All

Table 3. Displacement boundary conditions for running standard tests in a strain-controlled manner.

Test	Displacement boundary condition definition
Uniaxial	$U_1^{RP(1)} = \delta_\circ$
Biaxial	$U_1^{RP(1)} = U_2^{RP(2)} = \delta_\circ$
Planar	$U_1^{RP(1)} = \delta_\circ$, $U_2^{RP(2)} = 0$
Volumetric	$U_1^{RP(1)} = U_2^{RP(2)} = U_3^{RP(3)} = \delta_\circ$
Shear	$U_1^{RP(1)} = U_2^{RP(2)} = U_3^{RP(3)} = 0$, $U_1^{RP(5)} = \delta_\circ$

3.2. Micromechanical simulation results

The simulation results for effective stress-strain response under standard tests for unit cells of simple cubic (SC, "Grid"), body-centred (BC, "X"), body-centred cubic (BCC, "Star"), face-centred cubic (FCC, "Cross"), and Octet type are shown in Figs. 9 to 13, respectively. All unit cells are of size $15 \times 15 \times 15\ mm^3$ and a strut radius of $0.75\ mm$ with joint thickening effect. As in Section 2, an isotropic linear elastic material model with Young's modulus $E = 0.53\ MPa$, Possion's ratio $\nu = 0.49$ and density $\rho = 1120\ kg/m^3$ is used. The effective stress-strain curves are plotted for uniaxial, biaxial, planar and volumetric tests in both compression and tension, as well as simple shear. The effective lateral strain curves are also plotted in terms of the applied effective strain for uniaxial, biaxial and planar tests in both compression and tension. The effective stress response and effective lateral strain curves are plotted up to the effective strain 50% or the effective strain at the point of self-contact; whichever is smaller. The undeformed shape of unit cells and the deformed shapes corresponding to each of the standard tests are also displayed. The deformed shapes are coloured by the contour of the microscale Mises stress at the effective strain of 25%.

The effective stress-strain responses in Figs. 9 to 13 generally show a strong asymmetry in tension and compression. For all unit cell types, the effective tensile stress response in uniaxial, biaxial, planar and volumetric tension is dominated by the stretch of struts along the loading direction despite lateral buckling of struts normal to loading direction. On the other hand, the effective compressive response mainly represents the nonlinear buckling of struts subjected to compressive axial forces. As a result, the effective tensile stresses are generally an order of magnitude higher than the effective compressive stresses. Due to the linear elastic behaviour of the Tango+ material, the effective tensile stress response of unit cells is a linearly increasing curve with strain. An exception is the uniaxial tension of the BC unit cell, which shows a mild nonlinear increasing effective response with increasing effective uniaxial strain due to the gradual alignment of struts along uniaxial loading direction.

The uniaxial, biaxial and planar effective compressive stress responses of unit cells dominated by strut buckling show a nonlinear buckling behaviour. In particular, the buckling-dominated effective response starts with an initially linear effective stress response due to the elastic axial compression of struts up to the point of micro-buckling of struts. Due to the geometrical imperfections, the buckling in this case is not a sharp bifurcation in the solution of static equilibrium. Rather, it happens smoothly over a finite effective strain range followed by an effective stress plateau, or a moderate effective stress increase as in the case of the FCC unit cell. Unlike stiff metal lattices which show a sudden drop in load after buckling due to the inherent plastic or failure response of metals, the post-buckling effective stress response of soft unit cells is an effective stress plateau or a moderately increasing effective stress response. An exception in this case is the BC unit cell which shows no buckling-type response in uniaxial, biaxial and planar compression tests as its deformation in these tests does not involve strut buckling. Instead, a bending-dominated linear effective stress-strain response is observed in these tests due to just bending of struts. In the volumetric compression tests, all unit cells including BC demonstrate a buckling-type effective stress-strain response due to strut buckling.

The effective shear stress response is dominated by the stretch of diagonal struts along the direction of the maximum principal stress; despite the buckling of struts along the direction of the minimum principal stress. As a result, the effective shear stress response is linear and dominated by elastic strut stretching. An exception in this case is the SC unit cell without diagonal struts. The effective shear stress response of the SC unit cell shows a mild nonlinear increase due to strut bending.

The effective lateral strain curves demonstrate the Poisson effect identified by lateral expansion or contraction due to the applied compression or tension, respectively. In uniaxial, biaxial and planar compressive tests of all unit cells, except BC, the effective lateral strain is usually one order of magnitude smaller than the applied effective compressive strain. Such a limitation on effective lateral strain is imposed by the presence of edge and face struts which undergo axial tension in compressive tests. For the BC unit cell with no edge or face struts, the structure is free to laterally expand in compressive tests. On the other hand, in uniaxial, biaxial and planar tensile tests, large effective lateral strains in the order of and even larger than the applied effective strains are observed. Such large lateral effective compressive strains are due to the lateral buckling of edge and face struts undergoing microscopic axial compressive force. Again, the BC unit cell with no edge or face struts is free to laterally contract in tensile tests.

In summary, three different types of behaviours are observed for soft unit cells: stretch-dominated, bending-dominated and buckling dominated. The stretch-dominated behaviour is a linear effective stress-strain response dominated by the axial tension of struts. The bending-dominated behaviour is a mild nonlinear effective stress-strain response due to the bending of struts. The buckling-

dominated behaviour denotes a nonlinear buckling effective stress-strain response dominated by the nonlinear buckling of struts under axial compression. While stretch- and bending-dominated behaviours have been frequently characterized in previous studies [26, 23, 27], the buckling-dominated behaviour is specific to soft lattices, in which the moderately large buckling strains can be accommodated by elastic materials.

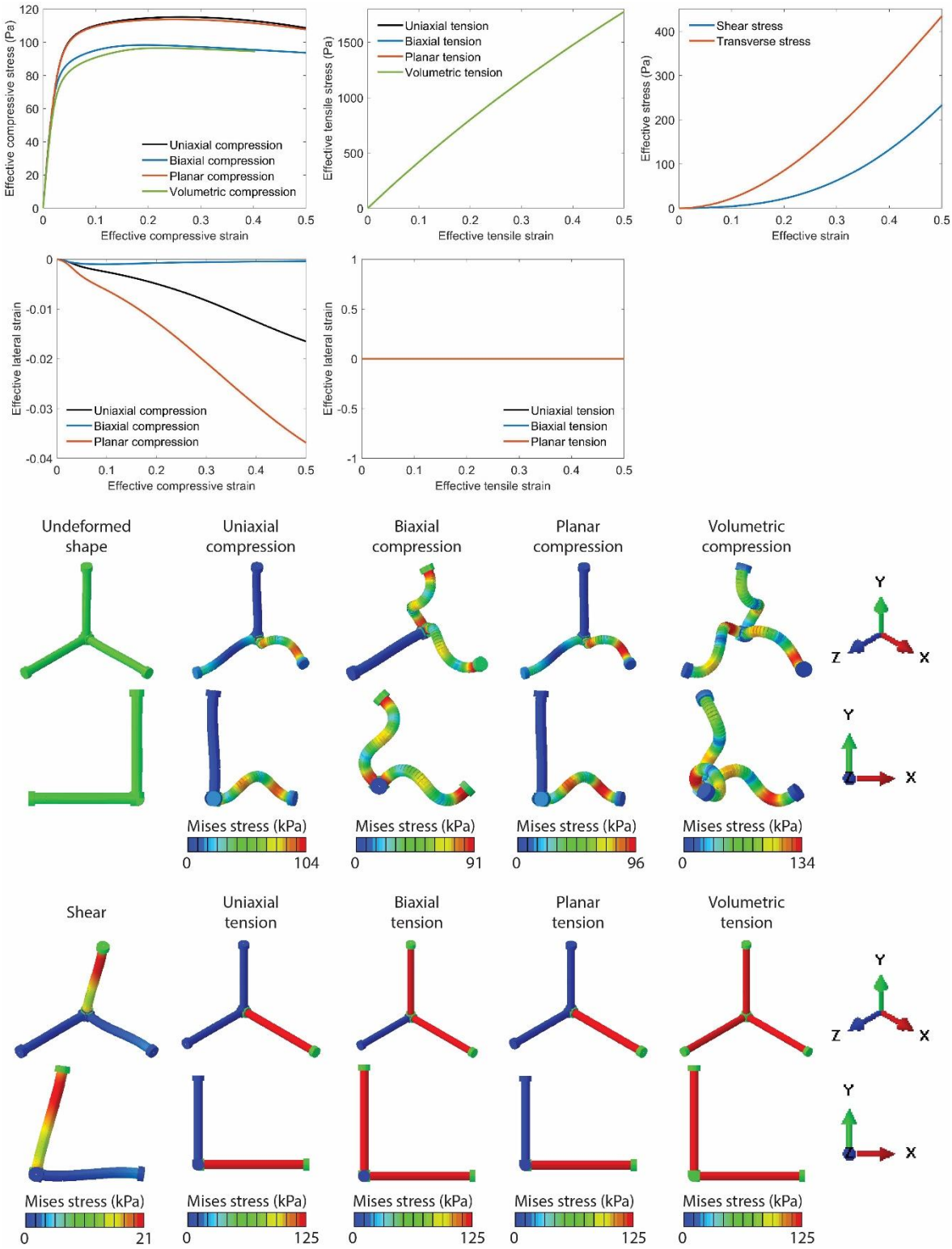

Fig. 9. Simulation results for standard tests on simple cubic (SC) unit cell under PBC, showing effective stress and effective lateral strain versus applied effective strain plots as well as the deformed shapes of unit cell coloured by the contour of the microscale Mises stress at the effective strain of 25%

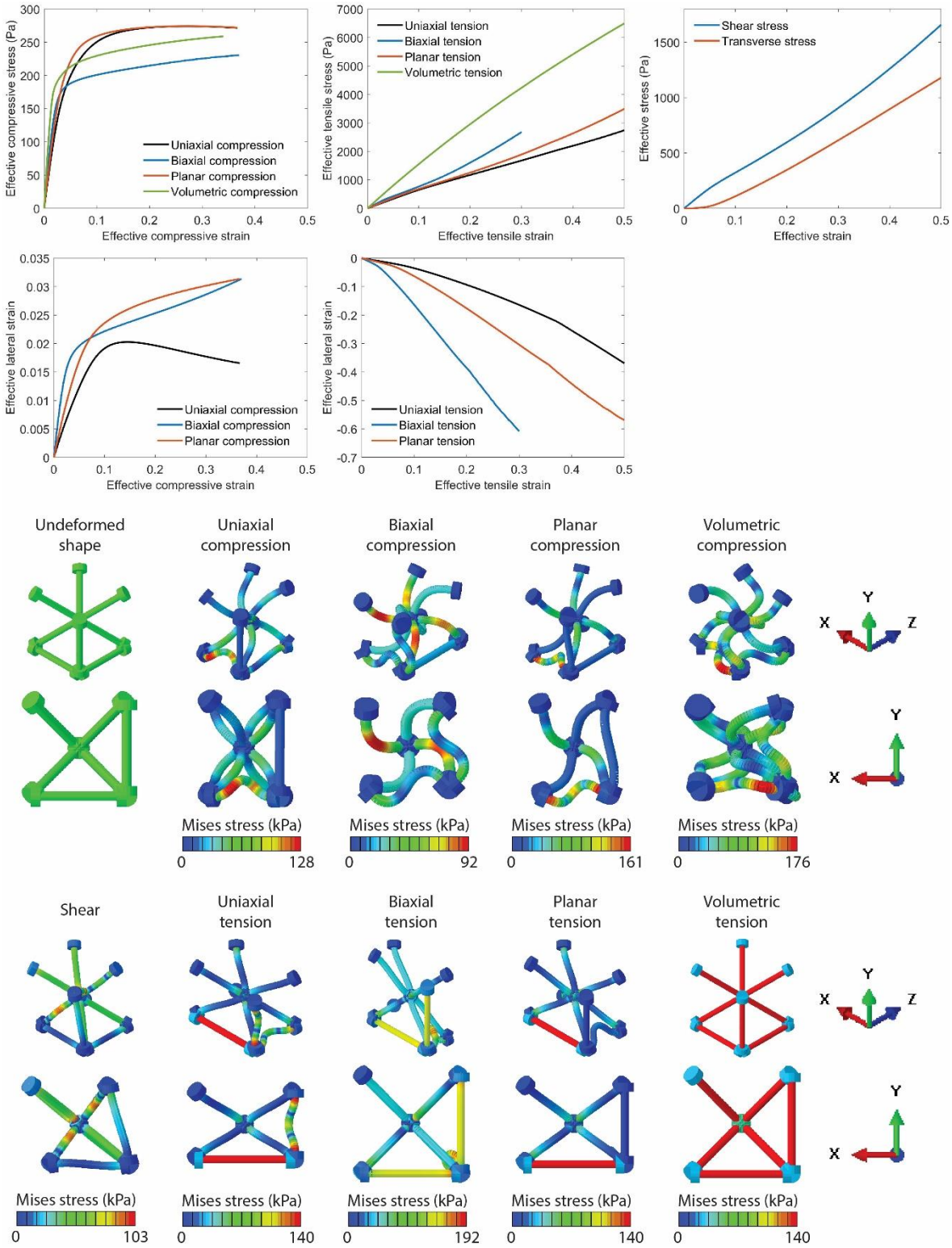

Fig. 10. Simulation results for standard tests on body-centred cubic (BCC) unit cell under PBC, showing effective stress and effective lateral strain versus applied effective strain plots as well as the deformed shapes of unit cell coloured by the contour of the microscale Mises stress at the effective strain of 25%

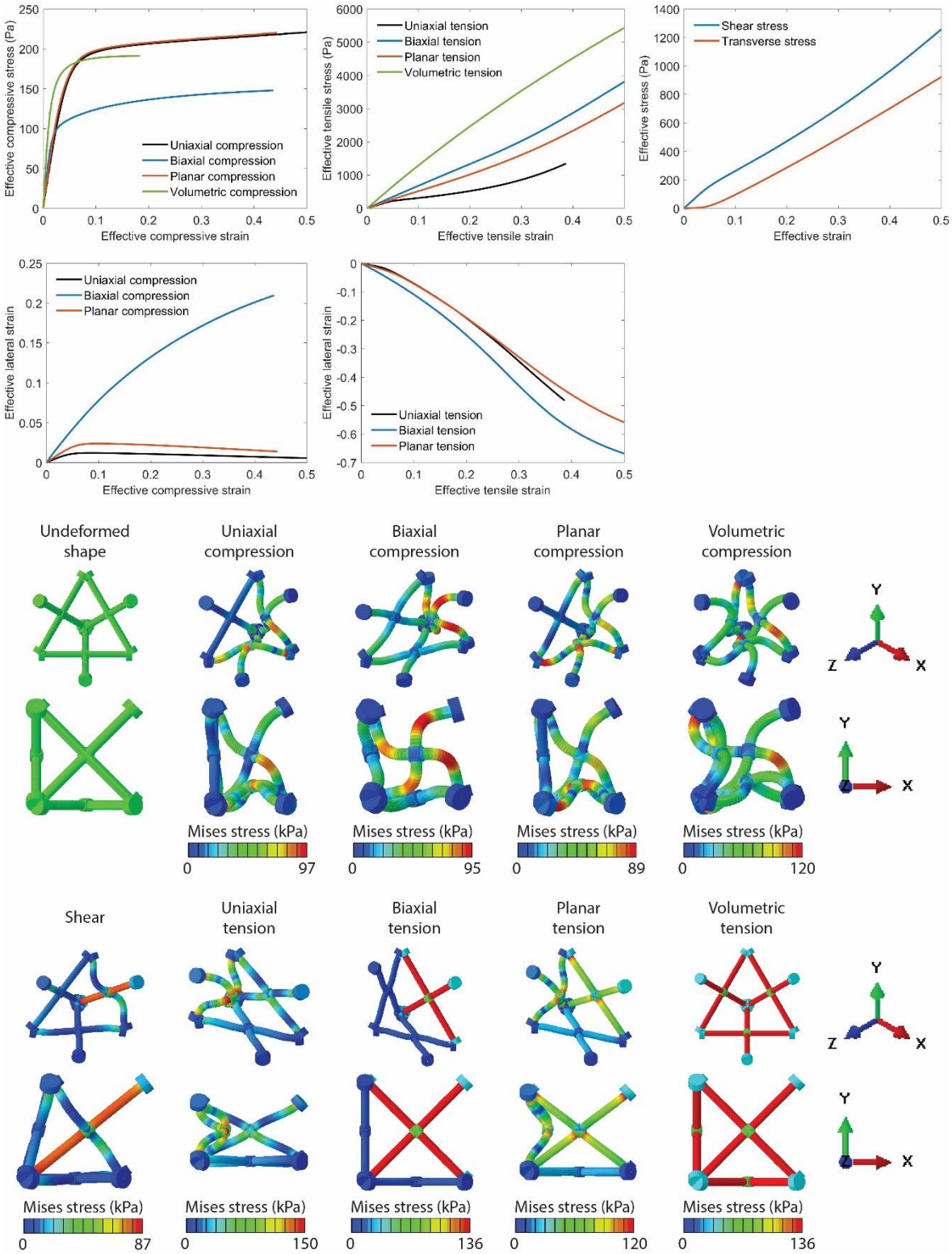

Fig. 11. Simulation results for standard tests on face-centred cubic (FCC) unit cell under PBC, showing effective stress and effective lateral strain versus applied effective strain plots as well as the deformed shapes of unit cell coloured by the contour of the microscale Mises stress at the effective strain of 25%

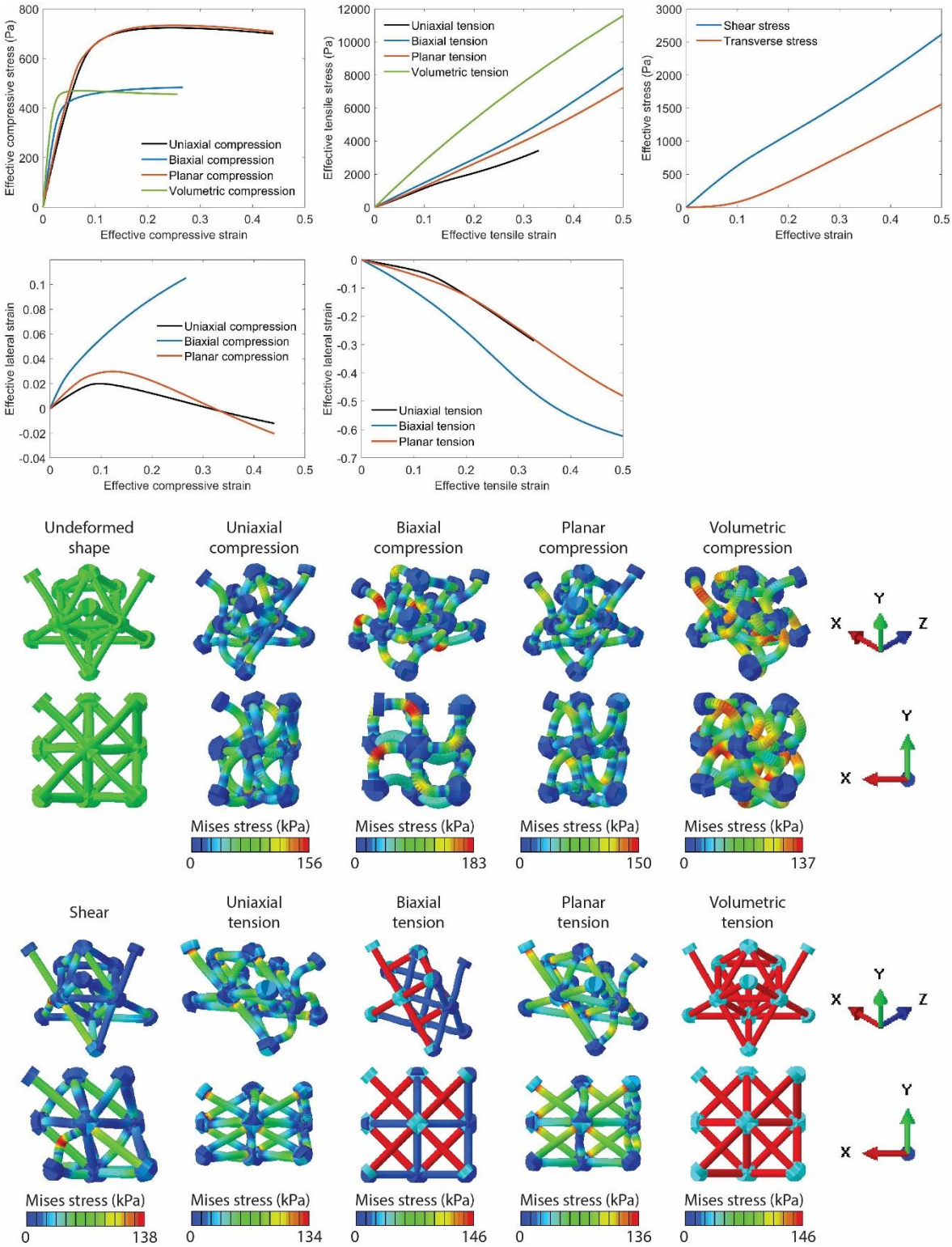

Fig. 12. Simulation results for standard tests on Octet unit cell under PBC, showing effective stress and effective lateral strain versus applied effective strain plots as well as the deformed shapes of unit cell coloured by the contour of the microscale Mises stress at the effective strain of 25%

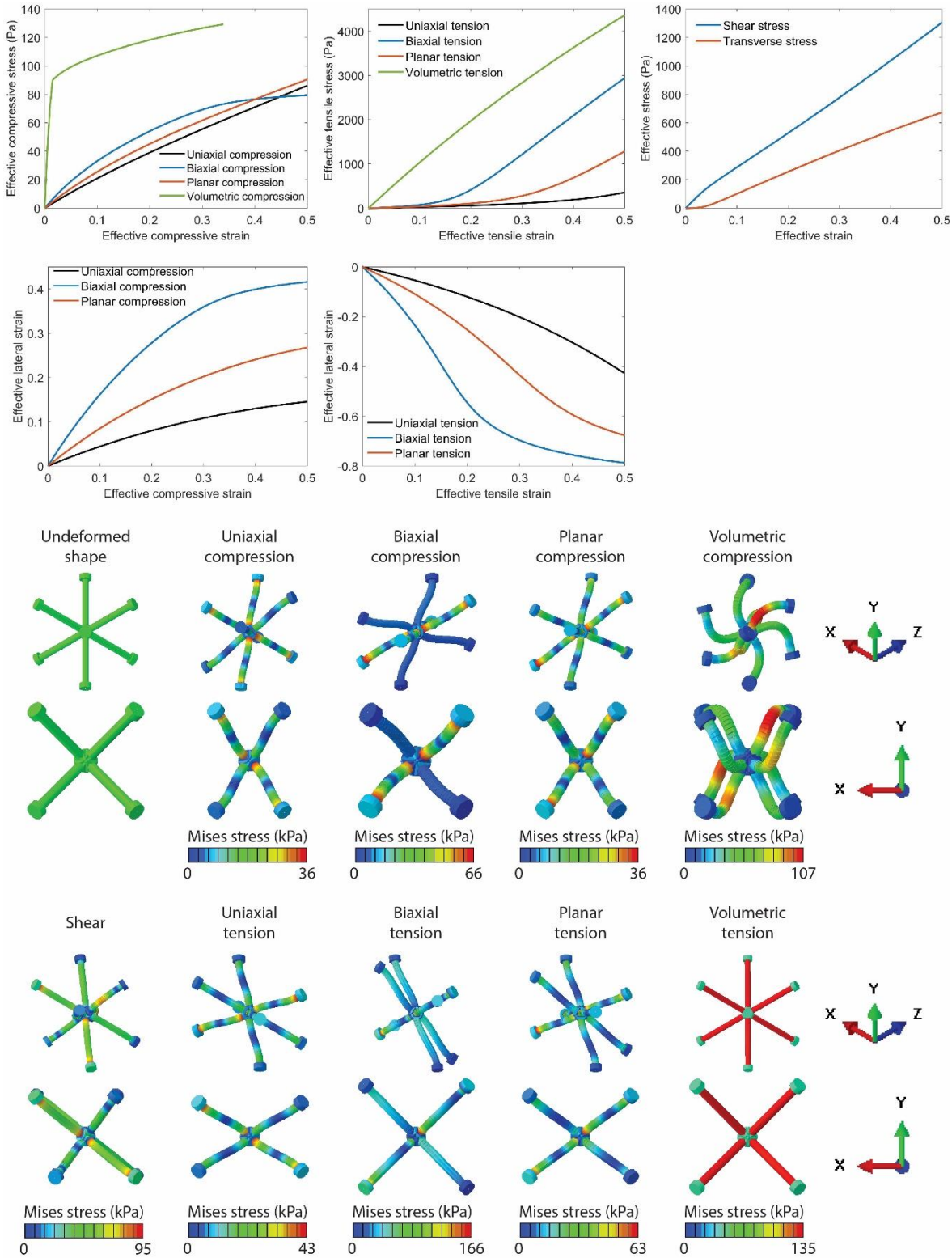

Fig. 13. Simulation results for standard tests on body-centred (BC) unit cell under PBC, showing

effective stress and effective lateral strain versus applied effective strain plots as well as the deformed shapes of unit cell coloured by the contour of the microscale Mises stress at the effective strain of 25%

4. Effective constitutive modelling of soft lattices

For the purpose of computationally efficient sequential multiscale simulation, explicit constitutive relations for the effective nonlinear elastic response of soft lattices are required. Such constitutive relations provide the effective stress tensor as a function of an effective deformation measure in the form of a closed form tensorial equation. The hyperelastic constitutive models, mainly developed for large-deformation nonlinear elastic behaviour of soft polymeric materials, can seemingly replicate the effective nonlinear elastic response of soft lattices. Hyperelastic models are described by a strain energy potential that defines the local strain energy density in terms of a deformation tensor. Our primary investigations on various hyperelastic models have shown that, among many, the hyperfoam material model [41, 42, 43], which was mainly developed for elastomeric foams, can be considered as a good candidate to predict the soft lattice behaviour, at least in the case of uniaxial loading. This hyperfoam model considers successive cell wall bending and elastic buckling in compression and successive cell wall bending and stretching in tension.

4.1. Hyperfoam model for uniaxial loading

In the absence of thermal strains, hyperfoam material model is described by the following strain energy potential

$$\Psi = \sum_{i=1}^{M} \frac{2\mu_i}{{\alpha_i}^2}\left[{\lambda_1}^{\alpha_i} + {\lambda_2}^{\alpha_i} + {\lambda_3}^{\alpha_i} - 3 + \frac{1}{\beta_i}\left(J^{-\alpha_i\beta_i} - 1\right)\right], \tag{1}$$

where $\lambda_1, \lambda_2, \lambda_3$ are the principal stretches and $J = \lambda_1\lambda_2\lambda_3$ is the elastic volume ratio, i.e., the Jacobian of the deformation gradient. The material parameter M indicates the order of the hyperfoam model. The material parameters μ_i, α_i, β_i determine the material stiffness, the shape of nonlinear stress-strain response, and the extent of material compressibility, respectively. These parameters are to be calibrated to the standard tests.

We investigate the applicability of the hyperfoam model to the effective behaviour of various unit cell types. For such an investigation, we focus on BC, BCC, and FCC unit cells as they represent three different kinds of effective stress-strain behaviour. All are stretch-dominated in tension, but in compression BC is bending-dominated, while BCC and FCC are buckling-dominated. Compared to BCC with very mild post-buckling strain softening, FCC shows post-buckling strain hardening in compressive tests.

Here, we present a discussion on the applicability of the hyperfoam model to the uniaxial behaviour of various unit cell types and leave the multiaxial behaviour for future study. Using Eq. (1), the hyperfoam model of order $M = 1$ is expressed by the following strain energy potential

$$\Psi = \frac{2\mu_1}{{\alpha_1}^2}\left[{\lambda_1}^{\alpha_1} + {\lambda_2}^{\alpha_1} + {\lambda_3}^{\alpha_1} - 3 + \frac{1}{\beta_1}\left(J^{-\alpha_1\beta_1} - 1\right)\right], \tag{2}$$

with three material parameters α_1, β_1, μ_1. Using Eq. (2), the nominal stress T_U along direction U is given in terms of the stretch λ_U along direction U as

$$T_U = \frac{\partial\Psi}{\partial\lambda_U} = \frac{2}{\lambda_U}\frac{\mu_1}{\alpha_1}\left({\lambda_U}^{\alpha_1} - J^{-\alpha_1\beta_1}\right), \tag{3}$$

where $J = \lambda_U \lambda_L^2$ with λ_L being the lateral stretch along the two directions normal to direction U. Using Eq. (3) in the lateral stress-free direction yields the following identity

$$\frac{2}{\lambda_L}\frac{\mu_1}{\alpha_1}\left(\lambda_L{}^{\alpha_1} - J^{-\alpha_1\beta_1}\right) = 0. \tag{4}$$

Combining Eq. (4) with Eq. (3) gives the uniaxial stress in terms of only uniaxial stretch as

$$T_U = \frac{2\mu_1}{\alpha_1}\lambda_U{}^{\alpha_1 - 1}\left(1 - \lambda_U{}^{-\alpha_1\frac{1+3\beta_1}{1+2\beta_1}}\right), \tag{5}$$

where $\lambda_U = 1 + \epsilon_U$ with ϵ_U being the uniaxial strain.

We fit Eq. (5) to the uniaxial stress-strain curves obtained in Section 3.2 to estimate the material parameters α_1, β_1, μ_1 for unit cells BC, BCC and FCC. Generally, the quality of a fit depends on the employed range of strain used for fitting. A limited fitting strain range, selected based on the range of strains experienced in the actual application, can result in a more accurate hyperfoam model. For example, in the case of sandwich structures for cushioning applications, the actual strains are compressive and fitting to just compressive test data results in a more accurate hyperfoam model. In order to investigate the strain range-dependent accuracy of the hyperfoam model, the uniaxial hyperfoam model is calibrated to the uniaxial test data for BC, BCC, and FCC unit cells over various strain ranges. Fig. 14 shows the fitting results for only uniaxial tension, only uniaxial compression, and uniaxial tension and compression test data in the strain ranges over which a satisfactory fit could be achieved.

Using either only uniaxial tension or only uniaxial compression test data, a very good fit is achieved for all unit cell types for the whole range of applied strain. In a general boundary value problem, where both tensile and compressive strains may occur, the fit is to reproduce the uniaxial test data in a range from compressive to tensile strains. Such a fit is shown in Fig. 14 for the selected unit cells BC, BCC, and FCC. For the BC lattice, which is not buckling-dominated in compression, a good fit is achieved in the whole applied strain range $-0.5 < \epsilon < 0.5$. However, for the BCC a satisfactory fit can be obtained in a more limited range of applied strain $-0.37 < \epsilon < 0.05$ corresponding to the approximately symmetric stress range $-271 < \sigma < 335$ Pa. Similarly, a very good fit is obtained for the FCC lattice in the applied strain range $-0.5 < \epsilon < 0.05$ corresponding to the symmetric stress range $-221 < \sigma < 224$ Pa. Due to the buckling-dominated behaviour of BCC and FCC in compression, it is generally difficult to determine a model that can capture both compressive and tensile behaviour well.

4.2. Parameterization of the constitutive model

For engineering design or simultaneous macroscale topology and mesoscale constituency optimization of soft lattices, computational modelling with unit cell scale-resolution using beam elements arises concerns about numerical stability, computational efficiency and robustness of numerical simulations. These concerns could be overcome by multiscale simulation with continuum constitutive relations for unit cell behaviour, which are parameterized in terms of the aspect ratio a of the cell, i.e., the ratio of strut diameter D over cell size L, $a = D/L$.

	Uniaxial	Uniaxial	Uniaxial tension and

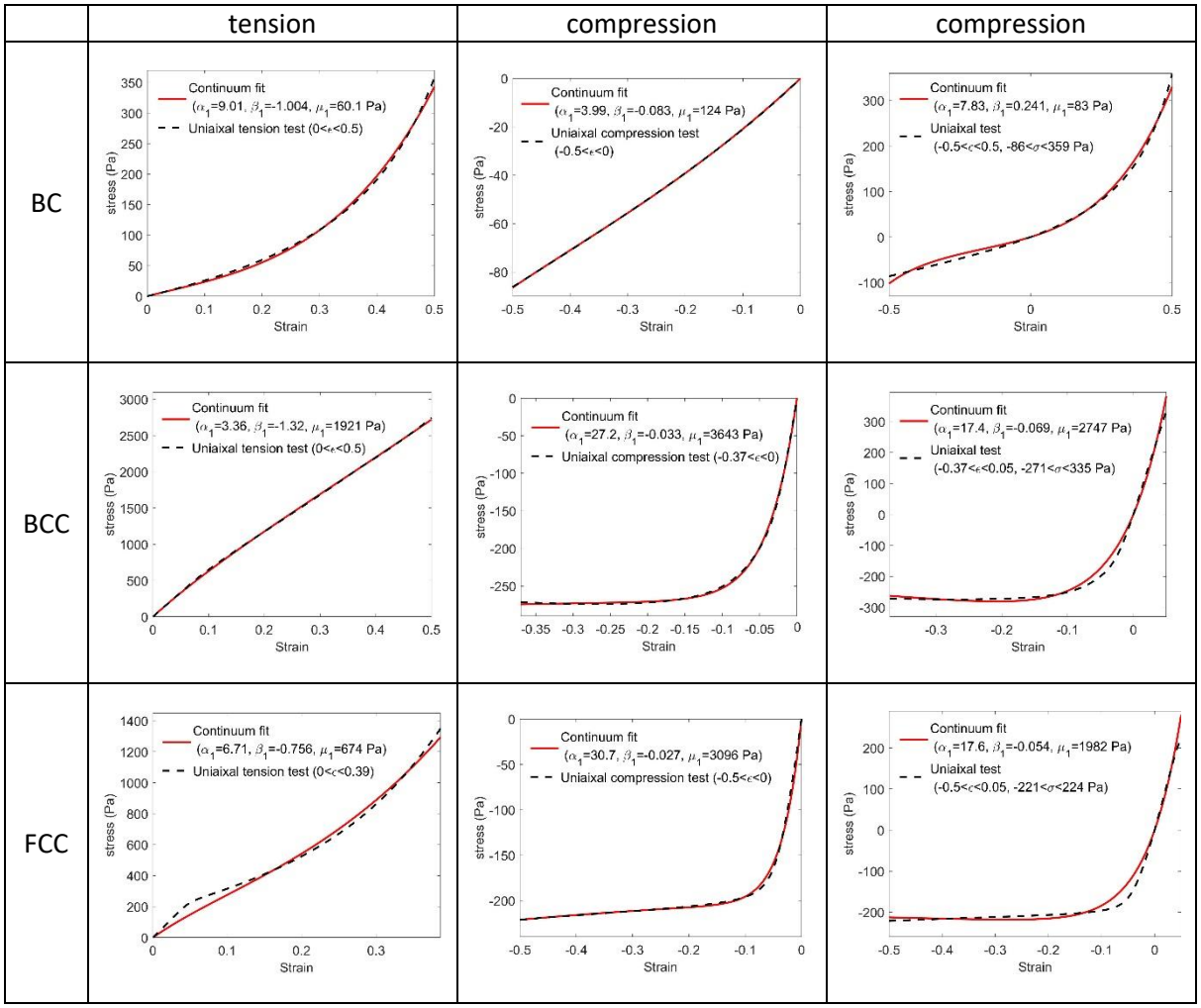

Fig. 14. Curve fitting of the uniaxial Hyperfoam model to only uniaxial tension, only uniaxial compression, and both uniaxial tension and compression test data for BC, BCC, and FCC unit cells. The uniaxial strain range and the Hyperfoam model parameters α_1, β_1, μ_1 used in curve fitting are shown in each plot.

Here, we investigate the dependency of the hyperfoam parameters α_1, β_1, μ_1 in the uniaxial test on the strut diameter D for BC, BCC, and FCC unit cells with fixed size $L = 15\ mm$. Following our previous discussion on the calibration of the hyperfoam model, see Eq. (1), and its parameters, the applicable uniaxial strain range is $-0.5 < \epsilon < 0.5$ for BC, $-0.37 < \epsilon < 0.05$ for BCC, and $-0.5 < \epsilon < 0.05$ for FCC. The calibrated hyperfoam parameters α_1, β_1, μ_1 are listed in Table 4 for different strut diameters $0.5, 1, 1.5, 2, 2.5\ mm$ for all unit cells. This data is used to plot the hyperfoam parameters α_1, β_1, μ_1 in terms of strut diameter D as shown in Fig. 15. For use in an optimization process, these data points can be interpolated to calculate the hyperfoam parameters for other values of strut diameter not listed in Table 4. Here, scalar functions are fitted to the data to express the hyperfoam parameters as functions of the aspect ratio, i.e., $\alpha_1(a)$, $\beta_1(a)$, $\mu_1(a)$. The specific forms of such functions which are plotted in Fig. 15 are given in Table 5.

These functions can be substituted in Eq. (3) or (5) to obtain the analytical relation for uniaxial stress response $T_U(a)$ in terms of the aspect ratio. Furthermore, they can be used in Eq. (2) to express the strain energy potential $\Psi(a)$ as a function of the aspect ratio. As to be expected from scaling laws for linear elastic moduli of lattices with stretching- and bending-dominated behaviour [23], the

modulus parameter μ_1 depends on a with exponents of around 2 to 4. For α_1 and β_1, linear and exponential relationships were used to obtain best fits. However, it is not immediately clear how these could relate to universal scaling laws. Nevertheless, these parameters can be used to pick a specific unit cell type and aspect ratio in order to tailor the nonlinear elastic response of a lattice structure. Furthermore, design and topology optimization methods could be used to computationally generate lattice structures with optimized microstructures.

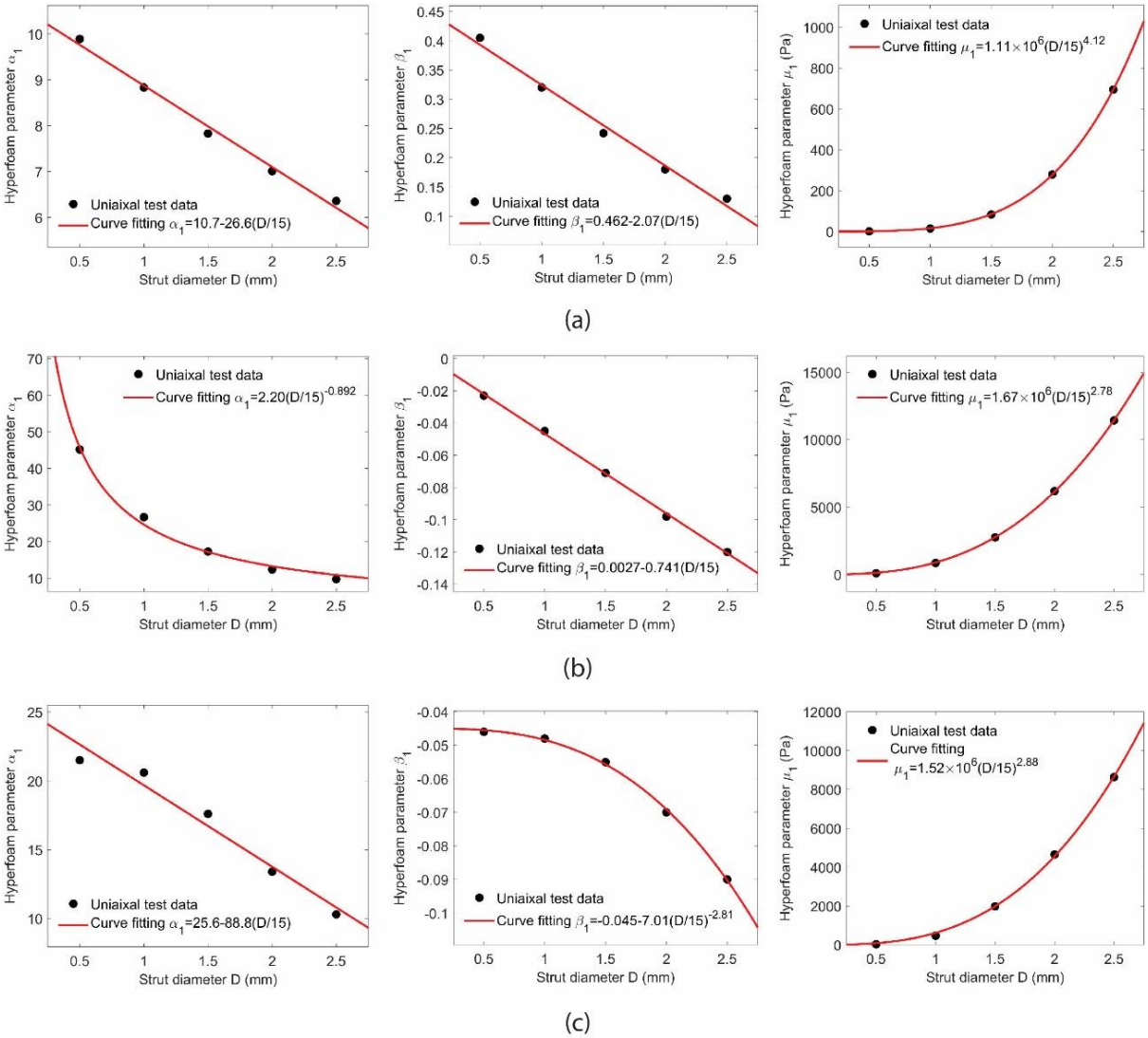

Fig. 15. Hyperfoam model parameters α_1, β_1, μ_1 as a function of strut diameter D for (a) BC unit cell, (b) BCC unit cell, (c) FCC unit cell. The fitting equation for each curve is also shown within the figure.

Table 4. Hyperfoam model parameters $(\boldsymbol{\alpha_1}, \boldsymbol{\beta_1}, \boldsymbol{\mu_1})$ for different values of strut diameter $\boldsymbol{D}$ or aspect ratio $\boldsymbol{a} = \boldsymbol{D}/\boldsymbol{L}$ for unit cells BC, BCC, and FCC

		BC			BCC			FCC		
$D\ (mm)$	a	α_1	β_1	$\mu_1\ (Pa)$	α_1	β_1	$\mu_1\ (Pa)$	α_1	β_1	$\mu_1\ (Pa)$
0.5	0.033	9.89	0.405	0.776	45.2	-0.023	97	21.5	-0.046	31.7
1.0	0.067	8.83	0.320	14.6	26.7	-0.045	853	20.6	-0.048	471
1.5	0.100	7.83	0.242	83.1	17.3	-0.071	2755	17.6	-0.055	1982
2.0	0.133	7.01	0.180	279	12.4	-0.098	6189	13.4	-0.070	4649
2.5	0.167	6.36	0.130	695	9.75	-0.120	11420	10.3	-0.090	8633

Table 5. Analytical functions for hyperfoam model parameters $(\boldsymbol{\alpha_1},\ \boldsymbol{\beta_1}, \boldsymbol{\mu_1})$ in terms of lattice aspect ratio $\boldsymbol{a} = \boldsymbol{D}/\boldsymbol{L}$ for unit cells BC, BCC, and FCC

Lattice	α_1	β_1	μ_1
BC	$\alpha_1(a) = 10.7 - 26.6a$	$\beta_1(a) = 0.462 - 2.07a$	$\mu_1(a) = 1.11 \cdot 10^6 a^{4.12}$
BCC	$\alpha_1(a) = 2.20a^{-0.892}$	$\beta_1(a) = 0.0027 - 0.741a$	$\mu_1(a) = 1.67 \cdot 10^6 a^{2.78}$
FCC	$\alpha_1(a) = 25.6 - 88.8a$	$\beta_1(a) = 0.045 - 7.01a^{2.81}$	$\mu_1(a) = 1.52 \cdot 10^6 a^{2.88}$

5. Continuum multiscale simulation and verification

To investigate the feasibility and computational efficiency of the proposed multiscale simulation approach, which is based on the micromechanical homogenization of lattice unit cells and the fitting of an effective hyperfoam continuum constitutive model, a comparative analysis of a sample lattice structure is performed with both full-scale beam and multiscale continuum models.

For this purpose, a BCC lattice structure composed of $5 \times 5 \times 5$ unit cells of size $15 \times 15 \times 15\ mm^3$ with a strut radius of $0.75\ mm$ is considered as a sandwich panel. As shown in Fig. 16, the compressive deformation of the lattice is simulated both by a full-scale 3D beam structure and by a 3D continuum model. As in Section 2, the beam model uses an isotropic linear elastic material model with Young's modulus $E = 0.53\ MPa$, Possion's ratio $\nu = 0.49$ and density $\rho = 1120\ kg/m^3$. The imperfect lattice model shown in Fig. 16b is constructed using the imperfection factor $\lambda_\circ = 0.075$ with total number of imperfection mode shapes $N_\circ = 360$. The hyperfoam material parameters for the continuum model are those shown in Fig. 14 for the BCC unit cell in uniaxial compression test. The continuum model is a solid cube of size $75 \times 75 \times 75\ mm^3$ meshed by Abaqus C3D8 8-node 3D brick elements of size $5 \times 5 \times 5\ mm^3$ to satisfy mesh convergence.

Fig. 16a shows the structural load-displacement response of both the beam and the continuum finite element models up to the compressive displacement of $15\ mm$, that is an overall structural strain of 0.2. Both models exhibit the same nonlinear behaviour, though the continuum model behaves slightly softer than the beam model. This offset can probably be attributed to the extra vertical boundary struts in the beam model compared to the continuum model. Considering the BCC unit cell in Fig. 10, the continuum model imitates a beam model created by laying $5 \times 5 \times 5$ unit cells which lacks the boundary struts existing on three positive faces of the beam model shown in Fig. 16b. Under uniaxial compression, these extra boundary struts along the uniaxial compressive direction contribute to the structural response and cause a stiffer structural response as compared to the

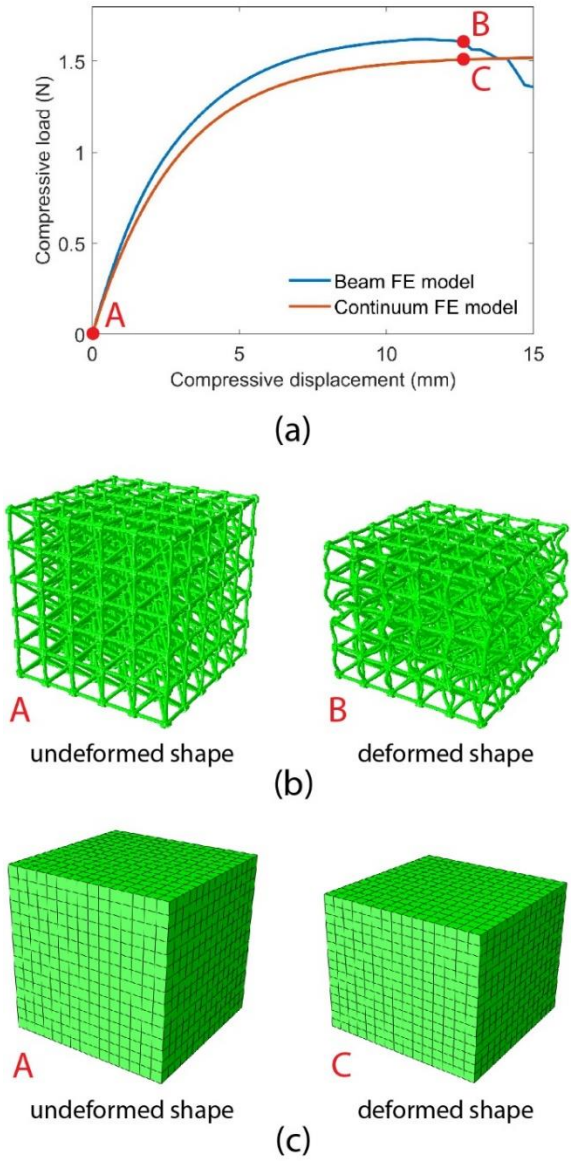

Fig. 16. Comparative study for the compressive deformation of a BCC lattice structure with $5 \times 5 \times 5$ cells simulated by both beam and continuum finite element models: (a) the structural load-displacement response, (b) the beam model, (c) the continuum model using the effective BCC hyperfoam constitutive model.

continuum model. It is expected that by extending the sandwich model dimensions along the in-plane directions normal to the uniaxial compressive direction, the effect of these boundary struts attenuates, and the continuum model response approaches the beam model response for sufficiently large sandwich structures.

Noteworthy in Fig. 16a is point B at which deformation localization happens due to the stress plateau and very mild strain softening in the compressive response of the BCC unit cell as shown in Fig. 10. Particularly, after reaching the post-buckling stress plateau, minor perturbations cause deformation localization and instability beyond point B shown in Fig. 16a. However, the continuum model cannot capture the strain localization phenomena as the constitutive stress response of the hyperfoam material model is strictly increasing. In addition, since self-contact is not considered in

our simulations, the structural stress response beyond point B is an approximation. Nevertheless, Fig. 16a still proves that the continuum hyperfoam model can reproduce the structural response of the lattice structure, at a much lower compactional cost. As an estimation of the computational expenses, the present beam model simulation, including linear buckling analysis and nonlinear static and dynamic analyses takes 20 hours on an Intel Core i7-7820X CPU, while the continuum model takes just a few seconds. As explained in section 2.3, much of the computational time for beam mode simulation is spent on the dynamic analysis. Particularly, the linear buckling analysis and the static analysis take 7 minutes and 14 minutes, respectively, and the rest is taken by the dynamic analysis.

6. Conclusion

We have addressed multiscale modelling of beam-lattice metamaterials at large elastic deformations, by focusing on their micromechanical nonlinear buckling behaviour, and evaluated their macroscopic, effective constitutive behaviour at finite strains.

For this purpose, we first proposed a computational model using shear-deformable nonlinear 3D beam finite elements for modelling large deformation response of soft lattices based on a global scalar imperfection factor that represents the average of all manufacturing geometric imperfections. For a specific soft lattice structure under prescribed loads and boundary conditions, the buckling mode shapes, scaled by the imperfection factor, were incorporated into the model as initial geometric imperfections. The resulting imperfect lattice model was then simulated to derive the nonlinear buckling response of the soft lattice. The total number of imperfection mode shapes was determined through a convergence analysis and the imperfection factor was estimated by calibrating the simulated response to the experimental structural load-displacement curve.

Using the validated nonlinear buckling analysis and periodic boundary conditions, the effective micromechanical behaviour of various unit cell types was investigated for typical material testing loading scenarios including uniaxial, biaxial, planar, and volumetric tension and compression, as well as shearing. Besides the well-known stretch- and bending-dominated behaviours of various unit cells under different loading conditions, it was observed that the compressive large deformation response of many unit cell types is buckling-dominated. The buckling-dominated response is initially linear due to elastic axial compression of struts up to the point of micro-buckling of the compressed struts, after which the stresses plateau or even decrease. This buckling-dominated behaviour is to be considered when designing lattice structures for large deformation, since it is very different from the stretch-dominated behaviour in the linear elastic infinitesimal strain regime.

As a first step towards facilitating nonlinear multiscale simulations of soft lattice structures, their macroscale, effective continuum constitutive modelling at finite strains was also investigated. For this purpose, the parameters of a hyperfoam constitutive model were fitted only to uniaxial strain test data. It was observed that either uniaxial compression or uniaxial tension behaviour, independently of each other, could be well replicated by the hyperfoam model. However, for buckling-dominated lattice types a common model, which is required for multiscale simulations subject to arbitrary loading scenarios, can only be obtained for a limited strain range. Furthermore, it was shown that the constitutive parameters of the hyperfoam model could be properly parametrized for varying aspect ratios of the unit cells.

Finally, a verification of the multiscale modelling framework was performed by modelling a $5 \times 5 \times 5$ BCC lattice structure both as a full-scale beam model and a 3D continuum multiscale

model using the effective hyperfoam constitutive model. At a much lower computational cost, the continuum model showed a good agreement with the beam model; which validates the effective constitutive modelling approach and demonstrates its efficiency.

From these results, future research directions can be concluded mainly in the area of macroscale constitutive modelling of soft lattices. While here only the uniaxial tensile behaviour was considered in the calibration of the hyperfoam model, a general nonlinear constitutive model with cubic symmetry shall be derived and investigated for soft lattice structures. Such a constitutive model can then be employed for nonlinear multiscale simulation and topology optimization of lattice structures subjected to large deformations.

Declaration of Competing Interest

The authors declare that they have no known competing financial interests or personal relationships that could have appeared to influence the work reported in this paper.

Acknowledgement

The authors acknowledge the support from the SUTD Digital Manufacturing and Design (DManD) Centre, funded by the Singapore National Research Foundation.

References

[1] J.-H. Lee, J. Singer and E. Thomas, "Micro-/Nanostructured Mechanical Metamaterials," *Advanced Materials,* vol. 24, no. 36, pp. 4782-4810, 2012.

[2] J. Plocher and A. Panesar, "Review on design and structural optimisation in additive manufacturing: Towards next-generation lightweight structures," *Materials & Design,* vol. 183, p. 108164, 2019.

[3] L. E. Murr, S. M. Gaytan, D. A. Ramirez and et al., "Metal Fabrication by Additive Manufacturing Using Laser and Electron Beam Melting Technologies," *J. Mater. Sci. Technol.,* vol. 28, no. 1, pp. 1-14, 2012.

[4] J. Wallach and L. Gibson, "Mechanical behavior of a three-dimensional truss material," *Int. J. Solids Struct.,* vol. 38, no. 40-41, pp. 7181-7196, 2001.

[5] R. Gümrük and R. A. W. Mines, "Compressive behaviour of stainless steel micro-lattice structures," *Int. J. Mech. Sci.,* vol. 68, pp. 124-139, 2013.

[6] D. W. Rosen, "Computer-Aided Design for Additive Manufacturing of Cellular Structures," *Comput. Aided Des. Appl.,* vol. 4, no. 5, pp. 585-594, 2007.

[7] S.-I. Park, D. W. Rosen, S.-K. Choi and C. E. Duty, "Effective Mechanical Properties of Lattice Material Fabricated by Material Extrusion Additive Manufacturing," *Addit. Manuf.,* Vols. 1-4, pp. 12-23, 2014.

[8] G. Dong, Y. Tang and Y. Zhao, "A Survey of Modeling of Lattice Structures Fabricated by Additive

Manufacturing," *ASME J. Mech. Des.,* 2017.

[9] L. Hao, D. Raymont, C. Yan, A. Hussein and P. Young, "Design and Additive Manufacturing of Cellular Lattice Structures," in *Proc. 5th Int. Conf. Adv. Res. Virtual Rapid Prototyping*, Leira, Portugal, 2011.

[10] C. Chu, G. Graf and D. Rosen, "Design for Additive Manufacturing of Cellular Structures," *Computer-Aided Design and Applications,* vol. 5, no. 5, pp. 686-696, 2008.

[11] Y. Jiang and Q. Wang, "Highly-stretchable 3D-architected Mechanical Metamaterials," *Sci. Rep.,* vol. 6, p. 34147, 2016.

[12] Y. Chen, T. Li, J. Zian, F. Scarpa, C.-W. Yao and L. Wang, "3D printed hierarchical honeycombs with shape integrity under large compressive deformations," *Materials & Design,* vol. 137, pp. 226-234, 2018.

[13] T. Chen, J. Mueller and K. Shea, "Integrated Design and Simulation of Tunable, Multi-State Structures Fabricated Monolithically with Multi-Material 3D Printing," *Sci. Rep.,* vol. 7, p. 45671, 2017.

[14] J. Liu, T. Gu, S. Shan, S. H. Kang, J. C. Weaver and K. Bertoldi, "Harnessing Buckling to Design Architected Materials that Exhibit Effective Negative Swelling," *Adv. Mater.,* vol. 28, no. 31, pp. 6619-6624, 2016.

[15] Y. Chen, F. Qian, L. Zuo, F. Scarpa and L. Wang, "Broadband and multiband vibration mitigation in lattice metamaterials with sinusoidally-shaped ligaments," *Extreme Mechanics Letters,* vol. 17, pp. 24-32, 2017.

[16] S. Babaee, J. Shim, J. C. Weaver, E. R. Chen, N. Patel and K. Bertoldi, "3D Soft Metamaterials with Negative Poisson's Ratio," *Adv. Mater.,* vol. 25, no. 36, pp. 5044-5049, 2013.

[17] A. Clausen, G. Wang, J. S. Jensen, O. Sigmund and J. A. Lewis, "Topology Optimized Architectures with Programmable Poisson's Ratio over Large Deformations," *Adv. Mater.,* vol. 27, no. 37, pp. 5523-5527, 2015.

[18] Y. Xie, X. Yang, J. Shen, X. Yan, A. Ghaedizadeh, J. Rong, X. Huang and S. Zhou, "Designing orthotropic materials for negative or zero compressibility," *International Journal of Solids and Structures,* vol. 51, pp. 4038-4051, 2014.

[19] N. G. Cheng, A. Gopinath, L. Wang, K. Iagnemma and A. E. Hosoi, "Thermally Tunable, Self-Healing Composites for Soft Robotic Applications," *Macromol. Mater. Eng.,* vol. 299, no. 11, pp. 1279-1284, 2014.

[20] Z. Ding, C. Yuan, X. Peng, T. Wang, H. J. Qi and M. L. Dunn, "Direct 4D printing via active composite materials," *Sci. Adv.,* vol. 3, p. e1602890, 2017.

[21] Z. Ding, O. Weeger, H. Qi and M. Dunn, "4D rods: 3D structures via programmable 1D composite rods," *Materials & Design,* vol. 137, pp. 256-265, 2018.

[22] O. Weeger, N. Boddeti, S.-K. Yeung, S. Kaijima and M. L. Dunn, "Digital Design and Nonlinear Simulation for Additive Manufacturing of Soft Lattice Structures," *Additive Manufacturing,* vol.

25, pp. 39-49, 2019.

[23] M. Ashby, “The properties of foams and lattices,” *Philosophical Transactions of the Royal Society A: Mathematical, Physical and Engineering Sciences,* vol. 364, no. 1838, pp. 15-30, 2006.

[24] L. Gibson and M. Ashby, Cellular Solids: Structure and Properties, Cambridge University Press, 1997.

[25] R. Lakes, „Materials with structural hierarchy,“ *Nature,* Bd. 361, pp. 511-515, 1993.

[26] V. Deshpande, M. Ashby and N. Fleck, “Foam topology: bending versus stretching dominated architectures,” *Acta Materialia,* vol. 49, no. 6, pp. 1035-1040, 2001.

[27] N. Huber, “Connections Between Topology and Macroscopic Mechanical Properties of Three-Dimensional Open-Pore Materials,” *Frontiers in Materials,* vol. 5, 2018.

[28] L. Liu, P. Kamm, F. García-Moreno, J. Banhart and D. Pasini, “Elastic and failure response of imperfect three-dimensional metallic lattices: the role of geometric defects induced by Selective Laser Melting,” *Journal of the Mechanics and Physics of Solids,* vol. 107, pp. 160-184, 2017.

[29] M. Potier-Ferry, „Foundations of elastic postbuckling theory,“ in *Buckling and Post-Buckling: Four Lectures in Experimental, Numerical and Theoretical Solid Mechanics*, Berlin, Heidelberg, Springer, 1987, pp. 1-82.

[30] Y. He, Y. Zhou, Z. Liu and K. Liew, “Buckling and pattern transformation of modified periodic lattice structures,” *Extreme Mechanics Letters,* vol. 22, pp. 112-121, 2018.

[31] M. Anderson, “Buckling of Periodic Lattice Structures,” *AIAA Journal,* vol. 19, no. 6, pp. 782-788, 1981.

[32] A. Nazir, A. Arshad and J.-Y. Jeng, “Buckling and Post-Buckling Behavior of Uniform and Variable-Density Lattice Columns Fabricated Using Additive Manufacturing,” *Materials,* vol. 12, no. 21, p. 3539, 2019.

[33] C. Coulais, J. Overvelde, L. Lubbers, K. Bertoldi and M. van Hecke, “Discontinuous Buckling of Wide Beams and Metabeams,” *Physical Review Letters,* vol. 115, no. 4, p. 044301, 2015.

[34] J. Overvelde, S. Shan and K. Bertoldi, “Compaction Through Buckling in 2D Periodic, Soft and Porous Structures: Effect of Pore Shape,” *Advanced Materials,* vol. 24, no. 17, pp. 2337-2342, 2012.

[35] L. Zhang, S. Feih, S. Daynes, Y. Wang, M. Wang, J. Wei and W. Lu, “Buckling optimization of Kagome lattice cores with free-form trusses,” *Materials & Design,* vol. 145, pp. 144-155, 2018.

[36] M. Geers, V. Kouznetsova, K. Matouš and J. Yvonnet, “Homogenization Methods and Multiscale Modeling: Nonlinear Problems,” in *Encyclopedia of Computational Mechanics*, John Wiley & Sons, Ltd., 2017.

[37] A. Vigliotti, V. Deshpande and D. Pasini, “Non linear constitutive models for lattice materials,” *Journal of the Mechanics and Physics of Solids,* vol. 64, pp. 44-60, 2014.

[38] H. Liu and J. Lv, “An equivalent continuum multiscale formulation for 2D geometrical nonlinear analysis of lattice truss structure,” *Composite Structures,* vol. 160, pp. 335-348, 2017.

[39] G. Philipot and D. Kochmann, “A quasicontinuum theory for the nonlinear mechanical response of general periodic truss lattices,” *Journal of the Mechanics and Physics of Solids,* vol. 124, pp. 758-780, 2019.

[40] L. Beex, R. Peerlings and M. Geers, “A quasicontinuum methodology for multiscale analyses of discrete microstructural models,” *International Journal for Numerical Methods in Engineering,* vol. 87, no. 7, pp. 701-718, 2011.

[41] R. Ogden, “Large deformation isotropic elasticity – on the correlation of theory and experiment for incompressible rubberlike solids,” *Proceedings of the Royal Society of London A. Mathematical and Physical Sciences,* vol. 326, no. 1567, pp. 565-584, 1972.

[42] R. Hill, “Aspects of invariance in solid mechanics,” *Advances in Applied Mechanics,* vol. 18, pp. 1-75, 1979.

[43] B. Storåkers, “On material representation and constitutive branching in finite compressible elasticity,” *Journal of the Mechanics and Physics of Solids,* vol. 34, no. 2, pp. 125-145, 1986.

[44] Y. Wang, H. Xu and D. Pasini, “Multiscale isogeometric topology optimization for lattice materials,” *Computer Methods in Applied Mechanics and Engineering,* vol. 316, pp. 568-585, 2017.

[45] C. Imediegwu, R. Murphy, R. Hewson and M. Santer, “Multiscale structural optimization towards three-dimensional printable structures,” *Structural and Multidisciplinary Optimization,* vol. 60, pp. 513-525, 2019.

[46] T. I. Zohdi and P. Wriggers, An Introduction to Computational Micromechanics, Berlin Heidelberg: Springer-Verlag, 2005.

[47] M. Geers, V. Kouznetsova, K. Matouš and J. Yvonnet, “Homogenization Methods and Multiscale Modeling: Nonlinear Problems,” in *Encyclopedia of Computational Mechanics*, Second Edition ed., E. Stein, R. Borst and T. Hughes, Eds., American Cancer Society, 2017, pp. 1-34.